Solar Physics
DOI: 10.1007/●●●●●-●●●-●●●-●●●●-●

A Tiny Eruptive Filament as a Flux-Rope Progenitor and Driver of a Large-Scale CME and Wave

V.V. Grechnev[1] · **A.M. Uralov**[1] · **A.A. Kochanov**[1] · **I.V. Kuzmenko**[2] · **D.V. Prosovetsky**[1] · **Ya.I. Egorov**[1] · **V.G. Fainshtein**[1] · **L.K. Kashapova**[1]

Received ; accepted

Abstract

A solar eruptive event SOL2010-06-13 was observed with the Atmospheric Imaging Assembly (AIA) on board the Solar Dynamics Observatory (SDO). The event has been extensively discussed in the contexts of the CME development and an associated extreme-ultraviolet (EUV) wave-like transient in terms of a shock driven by the apparent CME rim. We continue the analysis of this event and reveal the following new features in the genesis of the CME and associated MHD wave. (1) A hot 11 MK flux rope developed from the structures initially associated with a compact filament system. The flux rope sharply expanded with an impulsive acceleration of up to 3 km s^{-2} one minute before the hard X-ray burst and earlier than any other structures, reached a velocity of 420 km s^{-1}, and then decelerated to about 50 km s^{-1}. (2) The CME development was driven by the expanding flux rope. Closed coronal structures above the rope a) were sequentially involved in the expansion from below upwards, b) approached each other, and c) apparently disappeared to reveal their common envelope – the visible rim, which became the outer boundary of the cavity. The rim was probably associated to a separatrix surface of the magnetic domain, which contained the pre-eruptive filament. (3) The formation of the rim was associated with a successive compression of the structures in the upper magnetosphere of the active region into the CME frontal structure (FS). When the rim was formed completely, it looked like a piston. (4) The disturbance responsible for the consecutive CME formation episodes was excited by the flux rope inside the rim, and then propagated outward. EUV structures arranged at different heights started to accelerate when their trajectories in the distance-time diagram were crossed by the trajectory of the fast front of this disturbance. (5) Outside the rim and

[1] Institute of Solar-Terrestrial Physics SB RAS, Lermontov St. 126A, Irkutsk 664033, Russia email: grechnev@iszf.irk.ru email: uralov@iszf.irk.ru
[2] Ussuriysk Astrophysical Observatory, Solnechnaya St. 21, Primorsky Krai, Gornotaezhnoe 692533, Russia email: kuzmenko_irina@mail.ru

FS, the disturbance propagated like a blast wave. Its signatures were a type II radio burst and a leading portion of the EUV transient. Its main, trailing part was the FS, which consisted of swept-up 2.5 MK coronal loops on top of the expanding rim. The blast wave strongly decelerated and decayed into a weak disturbance soon afterwards, being not driven by the trailing piston, which considerably slowed down.

Keywords: Filament Eruptions; Coronal Mass Ejections; Shock Waves; Type II Bursts

1. Introduction

A solar eruptive event in active region (AR) 11079 at an approximate position of S21 W82 was comprehensively observed on 13 June 2010 from about 05:30 to 05:50 (all times are referred to UT) with the *Atmospheric Imaging Assembly* (AIA) on board the *Solar Dynamics Observatory* (SDO; Lemen *et al.*, 2012). Observations with the *Sun Earth Connection Coronal and Heliospheric Investigation* instrument suite (SECCHI; Howard *et al.*, 2008) on the *Solar-Terrestrial Relations Observatory* (STEREO; Kaiser *et al.*, 2008) from a different vantage point complement the picture of the event. This event has been extensively discussed in the contexts of the CME development (Patsourakos, Vourlidas, and Stenborg, 2010) and an associated extreme-ultraviolet (EUV) wave-like transient in terms of a piston shock driven by the apparent rim of the CME bubble (Ma *et al.*, 2011; Kozarev *et al.*, 2011; Gopalswamy *et al.*, 2012; Eselevich and Eselevich, 2012; Kouloumvakos *et al.*, 2014). Nevertheless, some important questions remain unanswered. It is still unclear where actually was the flux rope, how it evolved, and which properties it had. It is uncertain how the CME was formed and what were the progenitors of its structural components.

Patsourakos, Vourlidas, and Stenborg (2010) followed the lift-off of the CME bubble in the SOL2010-06-13 event. The authors detected an eruptive filament, whose rise caused the rise of surrounding loops which eventually formed an EUV cavity. They concluded that the bubble was formed from a set of pre-existing loops during the main flare phase, while the possible CME trigger lied in the rise and possible instability of the filament. The upper limit for the size of a possible pre-existing flux rope was estimated to be very small, about 20 Mm.

Eselevich and Eselevich (2013) approximately measured the expansion of rising coronal loops starting from about 30 Mm and found their sequential involvement in the motion from below upwards during the CME formation. The authors have not noticed the eruptive filament and proposed that the source of the CME was a magnetic tube emerging with a high speed from below the photosphere.

In spite of comprehensive high-resolution multi-wavelength observations by SDO/AIA and *Extreme UltraViolet Imager* (EUVI) on STEREO-A and many efforts applied by several researchers listed, the flux rope escapes detection so far. The origin and regime of the CME-related wave also remain conjectural. Based on a sophisticated thermodynamic MHD model, Downs *et al.* (2012) simulated a detailed evolution of the EUV wave in the 13 June 2010 event in realistic coronal

conditions. The authors concluded that its outer, propagating component had properties of a fast-mode wave, but their analysis could not ascertain the wave excitation scenario. In spite of a number of the studies devoted to the presumable shock wave in this event, it is still unclear where and how it developed.

Genesis of the flux rope, CME formation, and shock wave excitation scenario are common long-standing issues for many similar events. Addressing these issues promises reconciliation of existing concepts with observational challenges and progress in understanding eruptive events and underlying processes.

The basic guidelines to solve these problems are provided by the standard flare model ('CSHKP'; Carmichael, 1964; Sturrock, 1966; Hirayama, 1974; Kopp and Pneuman, 1976) and its later elaborations. According to Hirayama (1974), the flare current sheet forms due to the lift-off of a filament, whose eruption is driven by a magnetohydrodynamic (MHD) instability of an increasing current in the filament. This can be the torus instability governed by the Lorentz force (Anzer, 1978; Chen, 1989, 1996). A twisted flux rope can be formed from an initial sheared configuration like a filament (van Ballegooijen and Martens, 1989; Uralov, 1990; Inhester, Birn, and Hesse, 1992; Longcope and Beveridge, 2007). Observational studies confirm the formation of flux ropes during flares (see, *e.g.*, Asai *et al.*, 2004; Qiu *et al.*, 2007; Miklenic, Veronig, and Vršnak, 2009) and their concurrent impulsive acceleration (Zhang *et al.*, 2001; Temmer *et al.*, 2008, 2010). The accelerating flux rope must produce an MHD disturbance. Propagating into surrounding regions, where the fast-mode speed is lower, the disturbance must rapidly steepen into a shock (Grechnev *et al.*, 2011b, 2014b; Afanasyev, Uralov, and Grechnev, 2013), and then expand ahead of the CME like a decelerating blast wave for some time. If the CME is slow, then the shock eventually decays. Otherwise, the frontal part of the shock changes to the bow-shock regime.

These scenarios were indeed revealed in observations of different events, ranging from the GOES B class up to the X class (Meshalkina *et al.*, 2009; Grechnev *et al.*, 2011b, 2011a, 2013, 2015). The active role of filaments or similar structures as progenitors of flux ropes (Uralov *et al.*, 2002; Grechnev *et al.*, 2006a) was confirmed in observations (Grechnev *et al.*, 2014a, 2015).

The 13 June 2010 event presents an opportunity to confront the picture outlined above, which we develop, with different views of the authors, who studied this event previously. In this way, we endeavor to verify our scenarios and specify and elaborate some of conjectures widely invoked. For these purposes we have made a new in-depth analysis of the 13 June 2010 eruptive event, pursuing the major unanswered questions of the genesis of the flux rope and its properties; how was the CME formed; where and how was the wave excited. We have revealed the developing flux rope and the appearance of the impulsively excited wave inside the forming CME and studied some of their properties.

The fact that neither the development of the flux rope nor the appearance of the shock wave have been detected previously indicates that various temperature ranges should be examined. Special efforts should be applied to image processing in this way. Section 2 addresses these issues as well as our measurement techniques. Using them, in the next sections we analyze the observations and discuss the results. Section 3 considers the geometry of the CME bubble and the orientation of the flux rope. Section 4 is devoted to the flux rope. Section 5

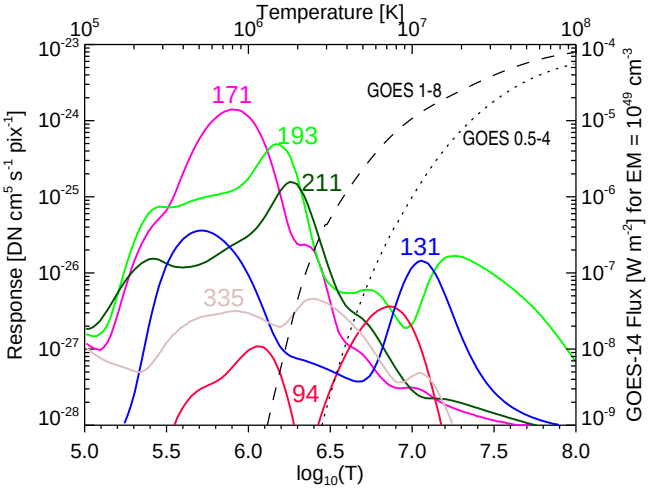

Figure 1. Temperature response functions for the six EUV channels of SDO/AIA that are dominated by iron emission lines calculated from the effective-area functions and assuming the CHIANTI model for the solar emissivity (adapted from Lemen *et al.*, 2012). The black broken lines represent the temperature response functions for the two GOES-14 channels.

analyzes the CME formation. Section 6 addresses the wave signatures. In Section 7 we try to understand the origin of the observed structures, compare our findings with a traditional view, and present an updated scenario of an eruptive event inferred from the observations. Section 8 summarizes the outcome from our analysis, outlines its implications, and finishes with concluding remarks.

2. Methodical Issues

2.1. SDO/AIA Images and their Processing

The major observational data we use came from SDO/AIA. Figure 1 shows the temperature response functions for the six EUV channels of AIA dominated by iron emission lines (Boerner *et al.*, 2012; Lemen *et al.*, 2012) along with the responses of the two GOES-14 channels. The 171 and 193 Å channels sensitive to normal coronal temperatures have been well known due to an extensive experience with SOHO/EIT, TRACE, and STEREO/EUVI data. The temperature response of the 211 Å channel resembles the major peak of the 193 Å channel shifted to 2 MK but lacks a minor high-temperature peak. The 94 and 131 Å channels have two temperature sensitivity windows. The lower-temperature windows are sensitive to normal coronal temperatures, and the higher-temperature those have peaks at 6.3 and 10 MK, respectively. The 335 Å channel has a broader characteristic with a lower sensitivity than the channels listed; therefore, our usage of this channel is limited. We also use the 304 Å channel, which is sensitive to temperatures around 5×10^4 K, with a lesser contribution from hotter plasmas around 1.8 MK (Lemen *et al.*, 2012; Downs *et al.*, 2012).

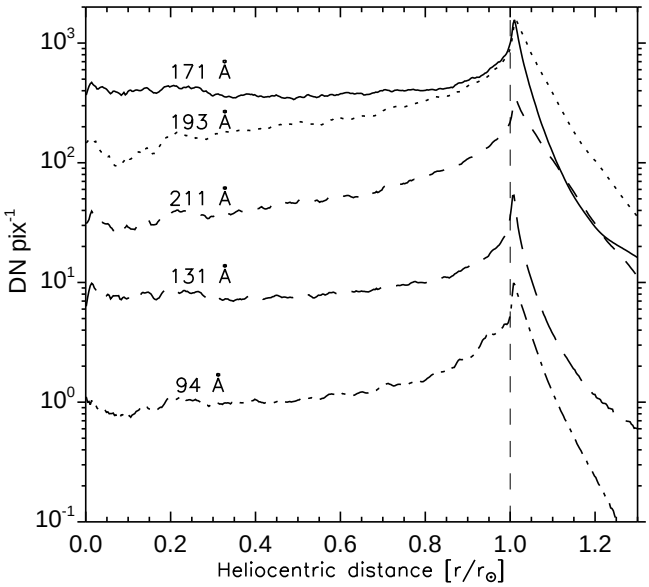

Figure 2. Azimuthally averaged radial brightness distributions computed from the solar images observed in five different channels of SDO/AIA. The plots are related to the actual exposure times of 2.9 s.

Due to the location of the active region close to the limb, the erupting features were observed by AIA against the off-limb background. It has a considerable diffuse component, whose brightness is maximum at the limb and decreases with height. This diffuse background substantially reduces the contrast of the erupting features. In addition, their brightness, I, dramatically decreases in their expansion; with a conserved number of emitting particles, the brightness depends on a linear size, r, as $I \propto r^{-5}$ (Uralov *et al.*, 2014; Grechnev *et al.*, 2015). Such widely used ways as subtracting of an earlier image of dividing by it do not reveal static features and contain traces of the base image.

We have computed averaged brightness distributions from solar images observed in different channels of SDO/AIA. The computation was made from ten averaged pre-event images in each channel using a ring scanning with a progressively increasing radius (see Kochanov *et al.*, 2013). This way is still not perfect because of strong differences between the low-latitude corona and regions above polar coronal holes. Nevertheless, the azimuthally averaged radial brightness distributions presented in Figure 2 allowed us to considerably enhance the appearance of off-limb features.

The plots reflect the coronal density distribution with a probable instrumental contribution due to a point spread function and scattered light. The peaks occur from $1.0065R_\odot$ for 131 Å to $1.0130R_\odot$ for 193 Å. The on-disk part has a nearly secant shape, and the off-limb part falls off almost exponentially in the 193, 211, and 94 Å channels. The falloff in the 171 and 94 Å channels sensitive to cooler plasmas goes nearly exponentially up to about $1.1R_\odot$ and then slows down.

Subtraction of these background distributions enhances the contrast of off-limb features. Dividing by these distributions compensates for the upwards brightness decrease (probably, a similar way was used by Ma *et al.* (2011)). We use various combinations of both these ways.

2.2. Kinematic Measurements

The properties of eruptive structures and the causal relations between the underlying processes can be recognized from their velocities and accelerations. They are basically inferred from the observational distance–time measurements. An obvious straightforward way to find the velocity and acceleration is the differentiation of the experimentally measured distance-time points.

However, the measurements of eruptive features, which are usually faint relative to associated flare emission, are complicated by a rapid decrease of its brightness or opacity that leads to considerable positional uncertainties. The irregular appearance of the measured feature in the images causes a scatter of the inferred velocities and accelerations. The scatter is especially large when the outermost detectable feature is considered. Even the modern elaborations of the measurement techniques based on the direct differentiation of the experimental distance-time points (*e.g.*, Vršnak *et al.*, 2007; Temmer *et al.*, 2010) do not overcome this difficulty completely, because the difference between the measured and actual position is always unknown.

An alternative approach is based on the fitting an analytic function to the measurements. Its major advantage is that the kinematical plots are calculated by means of the integration or differentiation of the analytic fit, thus providing a smooth outcome, rather than the differentiation of the measurements, that gives an intrinsically scattered result. If the kinematics of an analyzed feature is basically understood and described theoretically, then the problem is to compute the parameters of the corresponding analytic function.

Warmuth *et al.* (2001) proposed that fast Moreton waves observed in the Hα line and considerably slower "EIT waves" observed in EUV at larger distances were due to the same decelerating fast-mode disturbances. To fit their propagation, the authors attempted to use the 2-order polynomial and a power-law fit. Grechnev *et al.* (2008b) pointed out that a freely propagating blast-wave-like shock, which spent its energy to sweep up the plasma with a radial power-law density falloff, $n(r) \propto r^{-\delta}$, and extrude it from the volume it occupied previously, indeed had a power-law kinematics, $r(t) \propto t^{2/(5-\delta)}$. This simple approximation turned out to satisfactorily fit various wave signatures such as "EUV waves", type II bursts, and leading edges of fast CMEs (see, *e.g.*, Grechnev *et al.* 2011b, 2011a, 2013). A detailed description of the power-law fit and its usage in the analyses of the imaging data and dynamic radio spectra can be found in Grechnev *et al.* (2014b).

For the kinematics of CME structures, which have been completely formed and acquired maximum accelerations, we use analytic equations obtained in a self-similar approximation (Uralov, Grechnev, and Hudson, 2005; Grechnev *et al.*, 2008b). This approximation is based on the fact that the relation between the propelling and retarding forces (magnetic pressure and tension, plasma pressure,

and gravity) applied to any element of the expanding CME, established after the completion of the impulsive acceleration stage, is then progressively decreased by the same factor with an increase of the distance from the expansion center (*e.g.*, Low, 1982). This approximation applies, as long as the aerodynamic drag force from the solar wind has a minor importance, *i.e.*, until the regime of the plasma extrusion by the CME bubble changes to the regime of the plasma flow around its outer surface. The self-similar equations are complex (Grechnev *et al.*, 2014b) and resemble hyperbolic functions in behavior.

The kinematics of eruptive features during the impulsive acceleration stage has not yet been well understood. In this case, a more or less suitable analytic function can be chosen from considerations based on the properties, which have already been established. One knows *a priori* that the initial velocity is typically small or zero, the final velocity is nearly constant, and the acceleration occurs impulsively within a certain time. Considerable short-time variations of the acceleration and velocity are not expected well after the impulsive acceleration stage. The particular shape of the acceleration pulse does not substantially affect the distance-time plot because of the double integration. A bell-shaped acceleration pulse meets these speculations. If a real distance-time plot considerably deviates from the kinematics described with a single acceleration pulse, then a combination of two (or more) pulses can be used.

This approach has been successfully used in several studies by different authors (*e.g.*, Gallagher, Lawrence, and Dennis, 2003; Sheeley, Warren, and Wang, 2007; Wang, Zhang, and Shen, 2009) as well as in our studies (Grechnev *et al.* 2011b, 2013, 2014a; Alissandrakis *et al.*, 2013). In our technique, the results of the fit are used as a starting estimate of the parameters of the acceleration, and then they are optimized to outline the eruption in a best way. Our ultimate criterion is to follow the analyzed feature as closely as possible in all of the images. The major source of the errors is the uncertainty in following the same moving feature, whose visibility progressively decreases.

The most important issue in our present study is the kinematics of the flux rope, which was even difficult to detect. We fit the measured projected heights of the flux rope, $h(t)$, with a smooth function that accounts for its acceleration and deceleration phases. We modified equation (1) from Sheeley, Warren, and Wang (2007) to the following two-pulse form:

$$h(t) = h(t_1) + \frac{1}{2}(v_{\rm f}^{+} + v_0^{+})(t - t_1) + \frac{1}{2}(v_{\rm f}^{+} - v_0^{+})\tau_1 \ln\left[\cosh(\frac{t - t_1}{\tau_1})\right] + \qquad (1)$$
$$h(t_2) + \frac{1}{2}(v_{\rm f}^{-} + v_0^{-})(t - t_2) + \frac{1}{2}(v_{\rm f}^{-} - v_0^{-})\tau_2 \ln\left[\cosh(\frac{t - t_2}{\tau_2})\right]$$

Here v_0 and $v_{\rm f}$ are the initial and final asymptotic values of velocity for the acceleration (+) and deceleration (−) pulses, t_1 and t_2 are the acceleration and deceleration center times, $h(t_1)$ and $h(t_2)$ are the corresponding heights, and τ_1 and τ_2 are the timescales of the acceleration and deceleration. The corresponding velocity, $v(t)$, is

$$v(t) = \frac{1}{2}(v_{\rm f}^{+} + v_0^{+}) + \frac{1}{2}(v_{\rm f}^{+} - v_0^{+})\tanh\left(\frac{t - t_1}{\tau_1}\right) + \qquad (2)$$

$$\frac{1}{2}(v_{\rm f}^{-}+v_0^{-})+\frac{1}{2}(v_{\rm f}^{-}-v_0^{-})\tanh\Big(\frac{t-t_2}{\tau_2}\Big)$$

The acceleration profile, $a(t)$, with the contributions from the two pulses is

$$a(t)=\frac{v_{\rm f}^{+}-v_0^{+}}{2\tau_1}\Big[1-\tanh^2\Big(\frac{t-t_1}{\tau_1}\Big)\Big]+\frac{v_{\rm f}^{-}-v_0^{-}}{2\tau_2}\Big[1-\tanh^2\Big(\frac{t-t_2}{\tau_2}\Big)\Big] \qquad (3)$$

We fit the analytic function $h(t)$ to the measured data using the Levenberg–Marquardt least-squares minimization (Levenberg, 1944; Marquardt, 1963) implemented by C.B. Markwardt in the *SolarSoft MPFIT* package. To evaluate the confidence intervals of the resulting fit, *i.e.*, to estimate the influence of the measurement errors on the inferred quantities (the velocity and acceleration profiles), we use a technique similar to the parametric bootstrap method. Numerous simulation runs are carried out to produce a large number of data sets, in which the measured data points are displaced by normally distributed pseudo-random numbers. Then we calculate the variance for the parameters of the fit. In this way, we also monitor the stability of the fit against noisy data.

The whole set of the parameters used in our fit is redundant, while $v_{\rm f}^{+}=v_0^{-}$ appears to be sufficient. We have to keep all of them to ensure a stable behavior of our fitting software in its present implementation.

2.3. Estimations of Plasma Parameters

Important information about the eruptive structures and their properties can be provided by their temperature and emission measure (EM). Qualitative judgments about the temperatures of the coronal structures observed by SDO/AIA can be done from their appearance in different channels with a reference to the temperature response functions in Figure 1. A detailed evolution of temperature and EM in hot structures emitting soft X-rays (SXR) can be estimated from the two SXR GOES channels in terms of the single-temperature model using the standard *SolarSoft* routines. If EM of an emitting structure is known, then, with its size found from the images, its density and mass can be estimated.

The most general way is the inversion of the differential EM (DEM) of the structures observed nearly simultaneously in different AIA channels. Actually, the image in each next AIA channel is produced 12 s after the preceding one. Eruptive features of our interest can acquire high speeds that causes their appreciable displacements in the AIA images even during the relatively short time intervals between them. To reduce the errors due to this effect, we resize the images produced in all of the AIA channels according to the measured kinematics of a feature in question, thus compensating for its motion. Practically we take two sets of the AIA images, one observed one time step before the time of interest, and the second – the next set, resize each image according to its observation time, and then interpolate each pair of the images in each channel to the required time. This procedure considerably improves the co-registration of the images.

In our analysis we use for reliability two different ways. These are the regularized inversion technique and software developed by Hannah and Kontar (2012; hereafter HK for brevity) and a faster algorithm developed by Plowman,

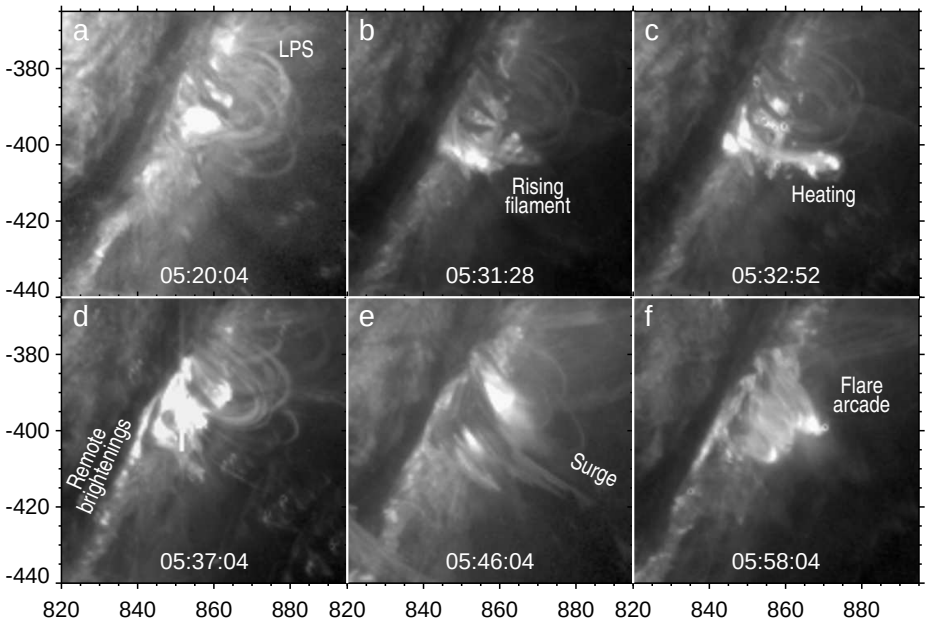

Figure 3. Activity in the low corona throughout the event observed in SDO/AIA 304 Å images. Label 'LPS' in panel (a) denotes a loop prominence system. The axes show hereafter the coordinates in arcsec from the solar disk center.

Kankelborg, and Martens (2013; hereafter PKM). Then we compare the results produced with the HK and PKM algorithms.

3. Geometry and Orientation

Figure 3 presents some episodes of the event observed in the SDO/AIA 304 Å channel. In a pre-event configuration in Figure 3a, a loop prominence system (LPS) is considerably inclined to the line of sight. LPSs are known to be located above the main magnetic polarity inversion (neutral) lines.

A rising filament in Figures 3b and 3c becomes bright which indicates its heating. Then the hot top of the filament becomes transparent and disappears later on. In Figure 3d, remote compact bright kernels intermittently appear and fade, being arranged in a direction nearly parallel to axis of the LPS. The plane of a dark surge in Figure 3e and the orientation of the flare arcade in Figure 3f also correspond to the inclined direction of the LPS.

3.1. Overall Configuration

Complementary observations from the STEREO-A vantage point make the overall configuration clearer. Figure 4 shows the 195 Å images produced by STEREO-A/EUVI in comparison with an SDO/HMI line-of-sight magnetogram (Figure 4b) and the flare ribbons visible in an SDO/AIA 1600 Å image (Figure 4d). The SDO data were transformed to the viewing direction from STEREO-A. A

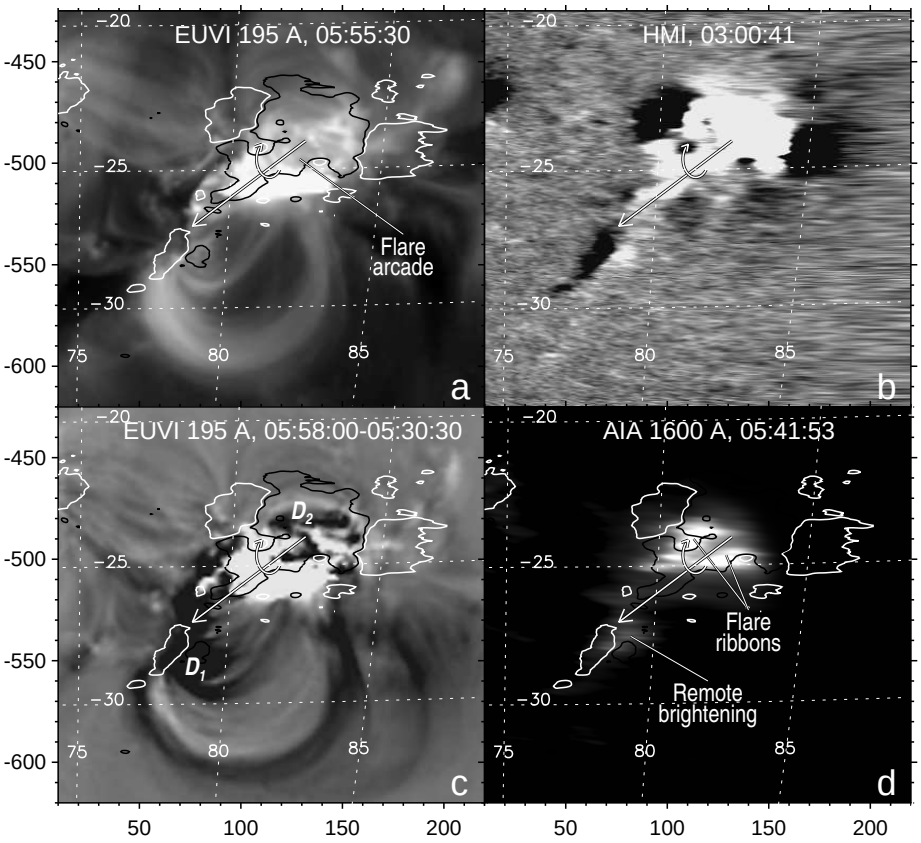

Figure 4. Flare configuration observed from STEREO-A along with contours of an SDO/HMI magnetogram transformed to this viewing direction. The contour levels correspond to −35 G (white) and +35 G (black) in the magnetogram smoothed with a 5-pixel boxcar. (a) Flare arcade in an EUVI 195 Å image. (b) Transformed HMI magnetogram within a range of ±50 G. (c) Dimmed regions in an EUVI 195 Å difference image. The dimming regions presumably associated with the footprints of the flux rope are denoted D_1 and D_2. (d) Flare ribbons and remote brightening in an SDO/AIA 1600 Å image transformed to the viewing direction from STEREO-A. The straight arrow indicates the orientation of the axial magnetic field in the flux rope (−37°). The round arrow shows the direction of the magnetic field in the arcade. The heliographic grid corresponds to viewing from Earth.

strong projection shrinkage of the flare site located near the limb reduces the quality of the transformed SDO images. The magnetic polarity in the westernmost part of the magnetogram appears to be inverted.

The orientation of the flare arcade (partly saturated) in a late EUVI image in Figure 4a corresponds to the flare ribbons in a transformed SDO/AIA 1600 Å image in Figure 4d. The ribbons must be separated by the magnetic neutral line, whose direction is shown by the straight tilted arrow (corresponding to the orientation of the LPS and arcade in Figure 3).

The difference image in Figure 4c reveals the regions of dimming, some of which are probably due to displacements of loops visible in Figure 4a or eruption of their neighbors. The core dimmings D_1 and D_2 might be associated with foot-

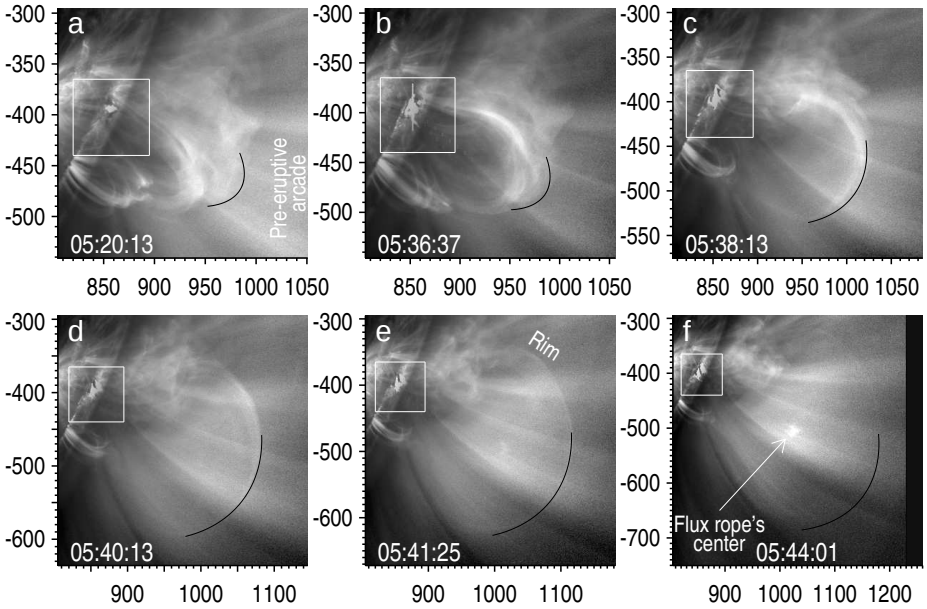

Figure 5. Development of the CME bubble in SDO/AIA 171 Å images. The images are progressively resized to keep the size of the outermost loop outlined by the black arc unchanged. The white frame corresponds to the field of view in Figure 3.

prints of the erupted flux rope (Hudson and Webb, 1997; Sterling and Hudson, 1997; Webb *et al.*, 2000; Mandrini *et al.*, 2005). This assumption is confirmed by the remote brightening in 1600 Å within D_1 in Figure 4d (see also Figure 3d). A conjugate footpoint of the flux rope must be within an opposite polarity; region D_2 meets this requirement. The direction of the flux rope's azimuthal magnetic field (the round arrow) should correspond to the flare arcade, being prompted by the magnetogram in Figure 4b, although considerably distorted.

The observations considered here indicate that the magnetic flux rope was, most likely, compact, with a length comparable to its width. The flux rope's axis was initially inclined by about $-37°$ to the East direction.

3.2. CME Lift-off

The eruption produced a CME, whose lift-off was observed by SDO/AIA in different-temperature channels. They reveal various coronal structures (see also the AIA_131_171_loops.mpg movie in the electronic supplementary material).

The 171 Å channel is sensitive to quiet coronal features of relatively low temperatures (see Figure 1). Figure 5 shows some episodes of the CME development in the AIA 171 Å images starting from the pre-event configuration in Figure 5a. The orientation of the pre-eruptive arcade in this panel appears to correspond to the inferred tilt of the flux rope's axis of $-37°$. The top of the visible set of the loops is outlined with the black arc.

As the developing CME lifts off, the arcade loops get involved in the expansion from below upwards (Patsourakos, Vourlidas, and Stenborg, 2010; Eselevich and

Eselevich, 2013). The rising lower loops press the overlying ones, and finally all of them apparently merge into a very thin, nearly circular rim. This process is addressed in detail in Section 5. Most authors, who studied this event previously, invoked a traditional assumption of the identity of the flux rope with the CME cavity, and related its outer boundary to the visible rim. The rim was considered as a visible cross section of the flux rope oriented nearly along the line of sight.

However, the rim in Figure 5e resembles a balloon with a thin skin or a soap bubble. With the inferred orientation of the flux rope, its cylindrical shape would not correspond to the appearance of the rim. Even though a possible rotation of the flux rope is not excluded, the appearance of the rim corresponds to a nearly spherical rather than cylindrical shape of the CME bubble.

The curvature of the black arc outlining the top of the arcade, which transformed into the rim, decreased in Figures 5a–5d. This effect was revealed by Patsourakos, Vourlidas, and Stenborg (2010), who termed it 'a lateral overexpansion'. Then the curvature gradually increased again in Figures 5e–5f, as the movie shows. The varying curvature will be discussed later. These figures also show a small bright kernel inside the bubble that might be a largest-opacity central part of the flux rope. This kernel also appears in 193 and 211 Å.

The AIA 211 Å images in Figure 6 reveal a low-brightness higher-temperature environment of the AR consisting of closed structures. They were located higher in the corona and had different orientations from the loops visible in 171 Å. The loops in 211 Å are faint in the pre-event image in Figure 6a and become discernible later (*e.g.*, in Figure 6e). The different orientations of the loops below the rim and above it suggest its association to a separatrix surface.

A separatrix surface prevents mixing magnetic structures, which belong to different magnetic domains isolated by this surface. Therefore, the expanding rim, being associated to a separatrix surface, limits the expansion of the loops below it. The rim sweeps up the coronal structures above it and leaves a rarefied volume behind. No dimming is pronounced in Figure 6, because we only reduced the structureless radially-varying coronal background in front of the bubble and behind it, without subtracting any preceding image.

The black arc outlines the top of the rim, and the white arc, whose radius is $90''$ larger, acceptably matches the outer edge of the pileup. Thus, the expansion velocities of the rim and the pileup from 05:40 to 05:44 were not much different.

North of the AR, a ray-like feature resembling a small streamer is denoted in Figure 6a. Presumably at its base, a quadrupole configuration is present in STEREO-A/EUVI 195 Å images about $100''$ west of the AR. This site is a candidate for a source region of a type II radio burst discussed in Section 6.

4. Flux Rope

4.1. Genesis and Expansion

According to Patsourakos, Vourlidas, and Stenborg (2010), the CME lift-off was possibly triggered by the eruption of a tiny filament ($\lesssim 20$ Mm). It is shown in Figures 3b and 3c. We start to search for the elusive flux rope from the activation of the filament observed in 131 Å.

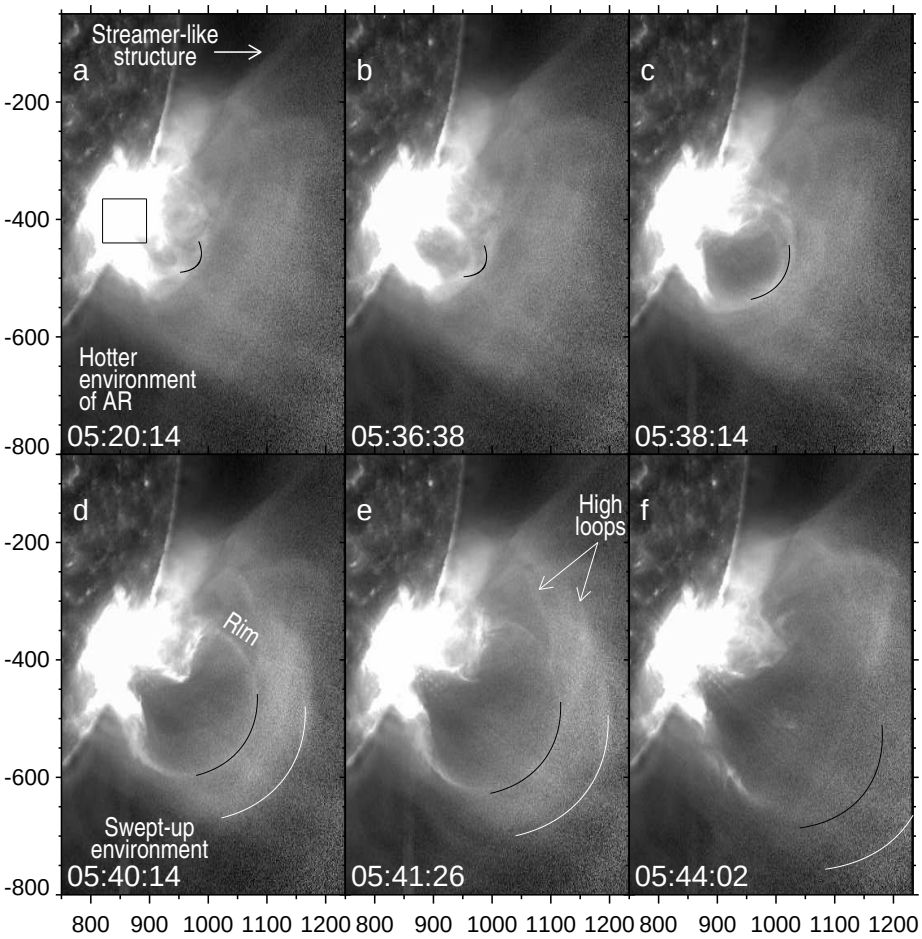

Figure 6. Development of the CME bubble in SDO/AIA 211 Å images. The black arc corresponds to the arc in Figure 5. The white arc in panels (d – f) is 90″ farther. The expanding rim sweeps up the bright structures enclosed between the arcs. The black frame in panel (a) corresponds to the field of view in Figure 3.

The initial dark filament (Figure 7a) activated in Figures 7b–7d. Figure 7e demonstrates the evolution of the event with time profiles recorded in two SXR GOES-14 channels and a light curve computed from the 131 Å images over a $153'' \times 153''$ region centered at $[855'', -396'']$ to encompass the flare site. This rather large area was chosen to collect the whole flare response, which was considerably broadened by an overexposure blooming effect. The gray vertical bars in Figure 7e represent the intervals, in which the images were averaged. The 131 Å light curve reveals a long gradual rise of the emission during 05:00–05:30 from the filament or its environment, indicating heating processes. This rise is not present in the GOES data related to the emission from the whole Sun.

A part of the filament activates and brightens up in Figure 7b that also indicates its heating. A similar appearance of the brightened filament in different

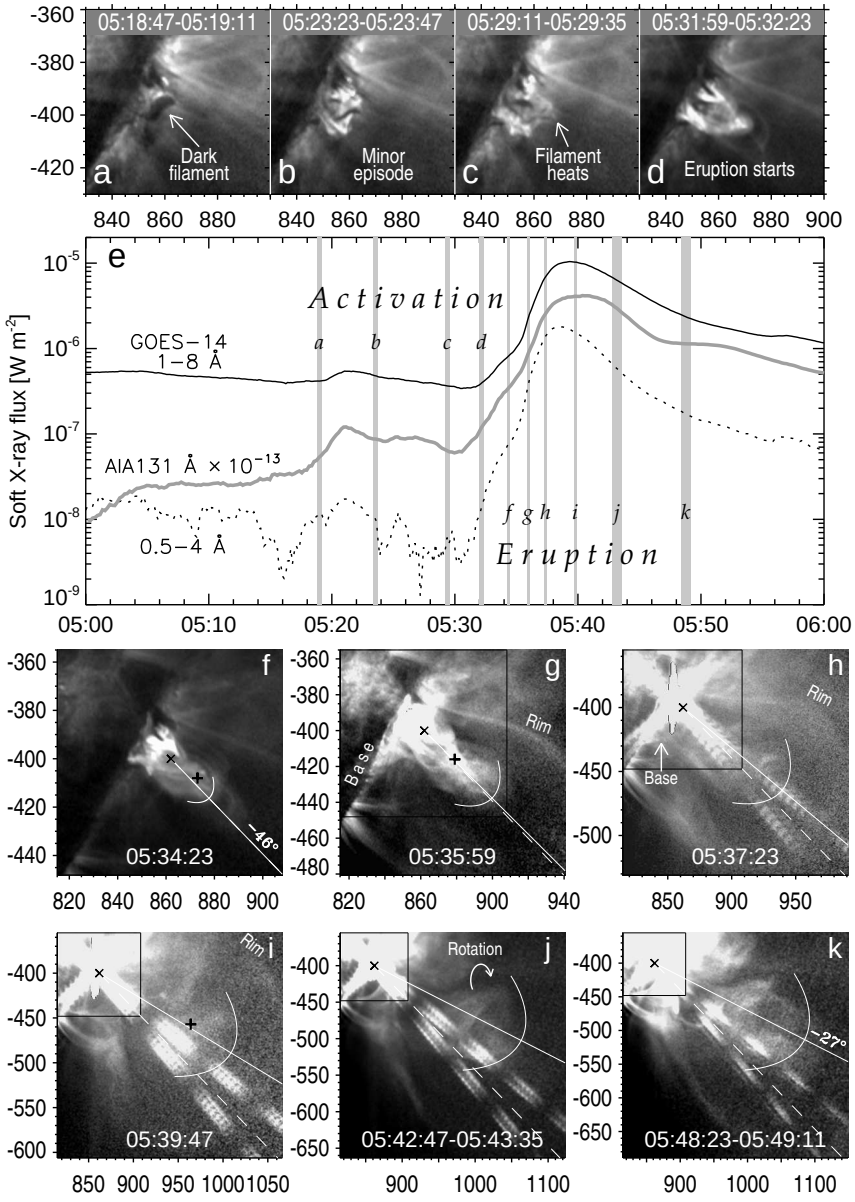

Figure 7. (a–d) Activation of the filament in averaged AIA 131 Å images. (e) GOES-14 SXR flux in 1–8 Å (black solid) and 0.5–4 Å (dotted) along with a gray light curve computed from AIA 131 Å images over the flare region. (f–k) Erupting flux rope in 131 Å images, which are progressively resized to keep the visible size of the rope unchanged. The arcs outline the flux rope's top. The solid line goes from the origin of the measurements (slanted cross) and the center of the flux rope. The dashed line corresponds to the initial orientation of the flux rope (−46° southward from the West). The thick straight crosses in panels (f), (g), and (i) denote the positions, for which DEM shown in Figure 9 was computed. The black frame corresponds to the field of view in panel (f). The images in panels (j) and (k) were averaged in the specified intervals after resizing. The coordinates are related to the middle of the averaging intervals.

AIA channels suggests a wide range of plasma temperatures in its body during this minor episode (05:20–05:24), preceding the major eruption. A response to this episode in 1–8 Å and even in 0.8–4 Å (although marginal) indicates that the filament brightening could be caught in the high-temperature window of the 131 Å channel (see Figure 1). The top of the filament in Figure 7c becomes bright and transparent. The eruption starts in Figure 7d.

From two GOES channels we estimated an average temperature of the brightened filament to be ≈ 6.6 MK and its total emission measure of $\lesssim 10^{48}$ cm^{-3} in the 05:20–05:24 episode (and, for the main flare, 15 MK and 6×10^{48} cm^{-3}). All of the estimates indicate that the 131 Å images are most promising to reveal the disappearing top part of the erupting filament, its possible relation to the flux rope, and the flux rope itself. The high-temperature window of the 94 Å channel could also be appropriate, but its sensitivity is considerably lower (see Figures 1 and 2). We therefore focus on the 131 Å images.

The emission flux in Figure 7e sharply increased after 05:30. The images become increasingly contaminated by strong overexposure effects such as saturation, blooming, and oblique diffraction patterns. Nevertheless, the image processing techniques described in Section 2.1 allowed us to detect an erupting flux rope in 131 Å. It is shown in Figures 7f–7k and the flux_rope_131.mpg movie. The images are progressively resized to keep the visible size of the flux rope unchanged by using the kinematical measurements described in the next Section. The arc outlines the top of the flux rope.

The body of the heated filament in Figure 7d transforms in Figure 7f into an erupting bundle of twisted loops. We ignore the poorly visible outermost group of the loops, which disappear soon. The bundle rapidly expands along the dashed line inside the rim, as the decrease of the black frame (field of view in Figure 7f) indicates. Several threadlike loops are apparently rooted to the base denoted in Figures 7g and 7h. As the rope lifts off, its Earth-facing base expands southeast, producing the remote birghtenings visible in Figures 3d and 4d.

The direction of the lift-off (solid line) gradually turns aside by $\approx 20°$. The flux rope rotates (see the circular arrow in Figure 7j and the movie). It is possible to see in latest images that more loops still erupt and join the flux rope. The latest visible loops are apparently injected into the northern part of the flux rope's bottom.

The picture described above is faintly visible in the 131 Å images (characteristic temperature 10 MK). To enhance the appearance of the flux rope in Figure 7, we had to average a few images within the specified intervals. The flux rope can also be detected in 94 Å (6.3 MK), but still poorer. These circumstances indicate that its temperature was around 10 MK.

4.2. Kinematics

To measure the kinematics of the expanding flux rope, we used a few different ways. The major difficulty in the measurements was its decreasing brightness, which became comparable with noises in the images, so that the flux rope eventually disappeared in latest images.

To get a hint at its final speed, we invoked the images produced with the SOHO's *Large Angle and Spectroscopic Coronagraph* (LASCO; Brueckner *et al.*,

1995). The center of the flux rope expanded in LASCO/C2 images after 09:30 with a speed of ≈ 52 km s^{-1}, while the speed of its top was considerably less than the asymptotic speed of the frontal structure, 190 km s^{-1} (Figure 15 in Section 5.2). The leading edge of the flux rope was about 30–40% ahead of its center visible in late AIA 193 Å images. These speculations indicate the final speed of $60 - 80$ km s^{-1} for the flux rope's top.

Using the results of preliminary measurements, we produced a movie, in which we scaled the field of view to compensate for the expansion of the flux rope. The movie made more specific its leading edge. If the visible size of the flux rope in the images still varied, then we revised our measurements and repeated the attempt. Various ways converged to the results presented in Figure 8.

The first-step direct manual distance–time measurements are presented in Figure 8a. The heights are related to the varying direction mentioned in the preceding Section. The assumption that the eruptive filament was a progenitor of the flux rope is confirmed by the coincidence of the filament's top measured from six AIA channels (while it was detectable, see the magnified initial part) with the top of the flux rope in the 131 Å images.

Secondly, we manually adjusted an acceleration profile composed from a positive pulse and a following negative one (Grechnev *et al.*, 2015). Thirdly, elaborating this approach, we developed the automatic fit described in Section 2.2. The black curve is its result. The shading represents the calculated uncertainties.

The fit is superimposed on a time-history image in Figure 8b (similar to the slit images used by Ma *et al.*, 2011; see also Alissandrakis *et al.*, 2013; Grechnev *et al.*, 2014a). Each column of this image is a spatial profile computed as averages over a 12-pixel ($7.2''$) wide slice extracted from a running-difference 131 Å image with a preceding by 48 s one. The instant orientations of the slices follow the turning flux rope. The expanding flux rope appears in this image as a bright strip. The fit should be its upper envelope. A bright feature visible above the fit from 05:31:30 till 05:36:00 is due to disappearing outermost loops seen in Figure 7f. They started to expand earlier and had a nearly constant speed.

Figure 8c presents the velocity–time plot computed from the analytic fit, the shaded uncertainty interval, and the GOES SXR flux. The speed of the flux rope started to conspicuously rise at 05:33, reached a maximum exceeding 400 km s^{-1} at 05:37, and then considerably decreased to ≈ 50 km s^{-1}. The velocity and SXR flux time profiles are similar in shapes and durations, with the SXR emission being delayed by 117 s relative to the velocity plot. The similarity of the rise phases appears to reflect the scenario of Hirayama (1974), in which the flare processes are driven by the erupting filament. The similarity of the declining parts is probably due to some expansion of the flare arcade in the wake of the expanding CME (Livshits and Badalyan, 2004).

Figure 8d shows the computed acceleration plot (thick black) with uncertainties, hard X-ray (HXR) flux recorded by the *Gamma-Ray Burst Monitor* of the *Fermi Gamma-ray Space Telescope* (Fermi/GBM; Meegan *et al.*, 2009) and reconstructed within the 25–50 keV energy band for this burst (thick gray); and the derivative of the GOES flux (thin). The flux rope underwent a strong acceleration up to 3 km s^{-2} $\approx 11 g_\odot$ ($g_\odot = 274$ m s^{-2} is the solar gravity

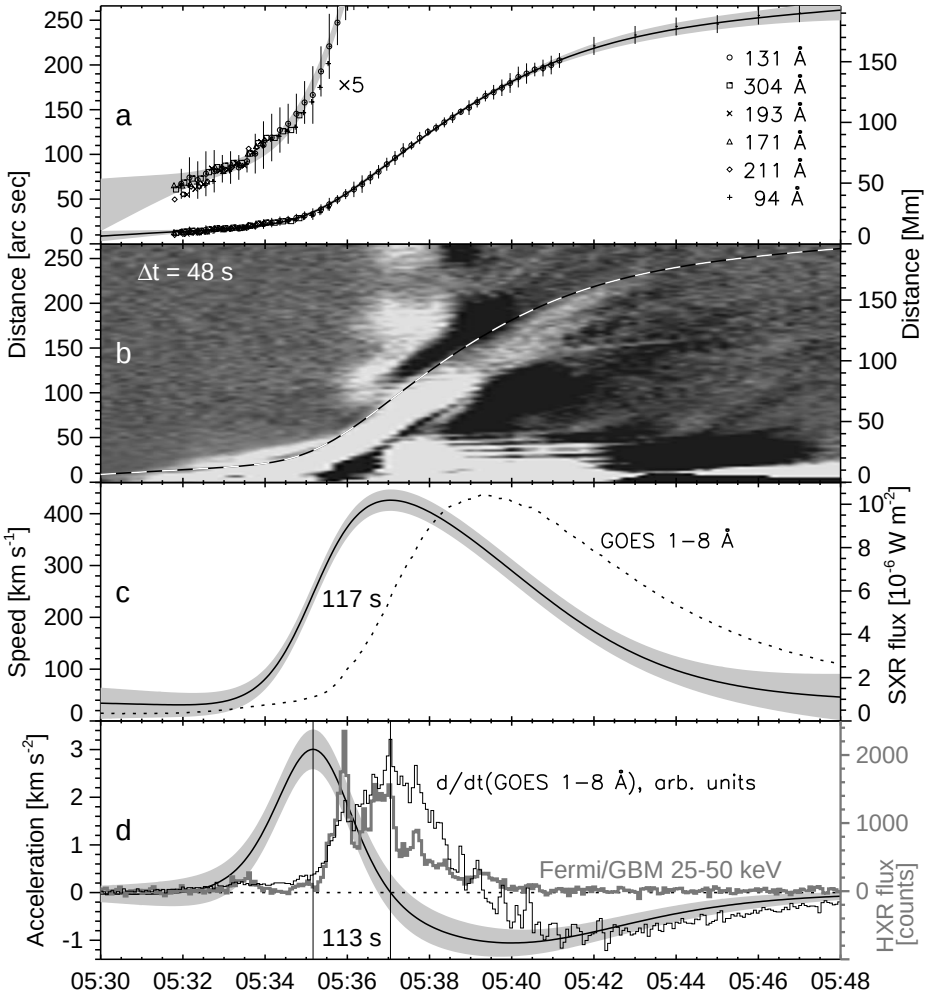

Figure 8. Kinematics of the flux rope. (a) Direct manual distance–time measurements (symbols) and the analytic fit (solid line). The initial part enlarged by a factor of 5 is also shown. The bars represent the errors of measurements from the 131 Å images estimated subjectively. The shadings in panels (a), (c), and (d) represent the uncertainties evaluated by the parametric fit. (b) One-dimensional time history of the flux rope's lift-off in 131 Å running-difference images separated by 48 s. The dashed line represents the analytic fit from panel (a). (c) Velocity–time plot computed from the analytic fit (solid) along with a GOES flux (dotted). (d) Acceleration of the flux rope (black), hard X-ray burst (gray), and the derivative of the GOES flux (thin).

acceleration at the photospheric level) peaking at 05:35:10. The acceleration changed to a longer deceleration, which reached -1 km s^{-2} at about 05:40:00.

The impulsively accelerating flux rope must have produced a considerable wavelike disturbance. Then the wave must propagate omnidirectionally, initially with a fast-mode speed, $V_{\rm fast}$. Typically, $V_{\rm fast} \gtrsim 10^3$ km s^{-1} in the low corona above active regions.

The time resolution of the Fermi/GBM data of an enhanced spectral resolution we use is 4 s. The time bins of the GOES-14 SXR data are 2 s. The positive portion of the derivative of the SXR flux roughly resembles the HXR burst (the Neupert effect; Neupert, 1968) and contains counterparts of most HXR features, but without a detailed correspondence. The derivative of the SXR flux is similar to the acceleration pulse, lagging behind it by 113 s. The lag of the HXR and microwave emissions by 1–2 minutes behind the acceleration of an eruptive structure seems to be a systematic phenomenon. We observed it previously in a few events (Grechnev *et al.* 2011b, 2013, 2015).

4.3. Differential Emission Measure

We computed DEM from sets of AIA images produced nearly simultaneously in different channels as described in Section 2.3. Figure 9 presents the results of the computations for three episodes of the flux rope development: its early appearance in Figure 7f (05:33:30, Figure 9a), the half-height acceleration in Figure 7g (05:35:30, Figure 9b), and during the deceleration stage in Figure 7i (05:39:02, Figure 9c). The times and central positions of the boxes, in which DEM was calculated, are specified in the upper-left corner of each panel. It was not possible to relate the calculations to the same part of the flux rope because of the sharp changes in its shape and strong overexposure distortions of the AIA images. The observation times, for which DEM was computed, are not identical to the most representative images of the flux rope in Figure 7.

The PKM profiles in the lower-temperature range in Figures 9a and 9b look not perfect, possibly, due to the strong instrumental distortions, while the HK profiles seem to be more plausible. Our major interest is related to the high-temperature domain (marked in Figure 9 by the shading). Here both methods supplied similar results, differing quantitatively in the maximum DEM by factors of 3.4, 2.9, and 0.58 for the three times, respectively. The temperature of the flux rope progressively increased from $\approx$ 10 MK at 05:33:30 to 12 MK at 05:35:00 and then to 17 MK at 05:39:02.

The widths estimated for the flux rope at 05:35:00 and 05:39:02 were about $d_2 \approx 21''$ and $d_3 \approx 120''$. If the total number of emitting particles inside the expanding volume was conserved, then the expected decrease of the brightness (*i.e.*, DEM; Grechnev *et al.*, 2015) should be $(d_3/d_2)^5 \approx 6100$. Actually, the DEM decrease from 05:35:00 to 05:39:02 was much less, 1200 (HK method) and 230 (PKM method). A similar situation was also between 05:33:30 and 05:35:00.

With known widths of the flux rope at the three different times, it is possible to estimate its density and mass. They are specified in the middle of the panels in Figure 9. Their ratios estimated for the hot component using the HK and PKM methods were 2.1, 1.1, and 0.89 at the three times. These differences seem to be tolerable because of the faintness of the flux rope.

All of the estimates converge to a considerable increase in the mass of the flux rope. Along with the increase of its temperature, this fact suggests an ongoing injection of hot plasma from the flaring region; otherwise, the temperature increase were challenging. As mentioned, the injection of high-temperature loops is indeed faintly visible at late stages of the eruption. It is possible that these

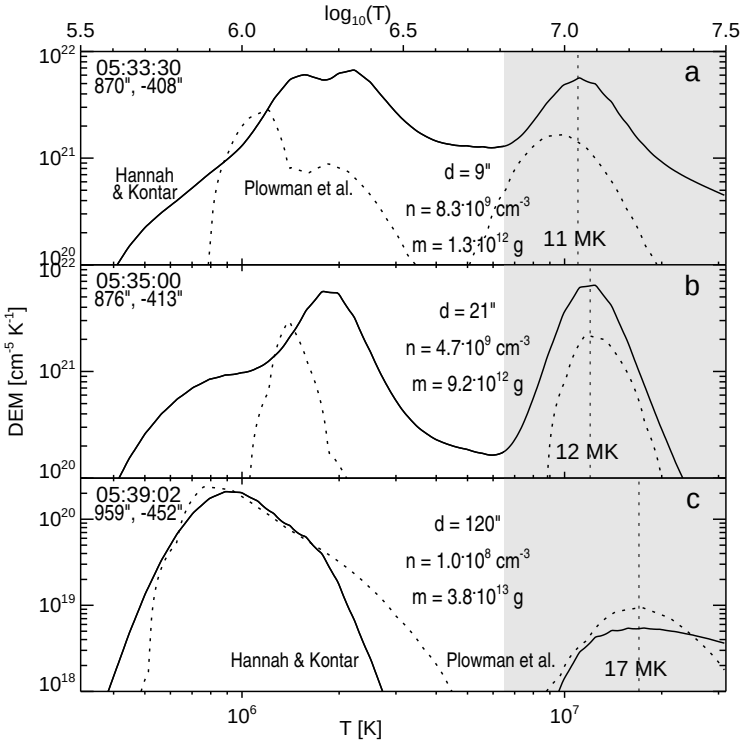

Figure 9. DEM temperature profiles in the flux rope at 05:33:30 (a), 05:35:30 (b), and 05:39:02 (c). The plots are related to the regions, whose centers are denoted by the straight crosses in Figures 7f, 7g, and 7i, respectively. Their coordinates are listed in the panels. The densities and masses were computed for the sizes, d, specified in the panels, within the shaded temperature range. DEM was computed using the HK (solid) and PKM (dotted) methods.

loops injected non-centrally also supplied a rotational momentum, causing the rotation of the flux rope indicated in Figure 7j and visible in the movie.

5. Development of CME Structural Components and Their Later Expansion

5.1. CME Formation in EUV Images

The phenomena observed during the CME lift-off in this event were analyzed by Patsourakos, Vourlidas, and Stenborg (2010); Eselevich and Eselevich (2013); and partly by Ma *et al.* (2011). Having not detected the eruptive flux rope, the authors nevertheless established a sequential involvement of coronal loops in the motion from below upwards during the CME lift-off. Here we study the relation between the erupting flux rope and the CME formation.

5.1.1. Rim and Inner Structures in 193 Å AIA Images

Figure 10 presents in five rows some episodes of the CME genesis (see also the AIA_131_171_loops.mpg movie). The eruptive flux rope visible in 131 Å is shown in the left column. The red arc outlines its top according to the measurements in Figure 8. This arc is also superimposed on the 193 Å images in the middle and right columns, where the flux rope is not visible. The middle column shows the 193 Å images with a reduced background (Section 2.1). They present the pre-eruptive coronal arcade above the AR. Four individual loops 1–4 are approximately outlined by the color oval arcs. The right column shows difference 193 Å images with preceding ones. The loops appear in these images, when start moving.

The right column of Figure 10 presents the development of the CME formation from below upwards, consistent with the conclusions of the preceding studies. This succession is confirmed by the progressively decreasing distances between loops 1–4. The agent, which drove the loops, was probably an outward-propagating MHD disturbance. The distance between the red and dark-green arcs in the middle column (*e.g.*, Figures 10f and 10i) also decreases; the flux rope (red) started to expand earlier and faster than the lowest loop 1 (dark-green). Thus, a probable driver of the expansion process forming the CME was the flux rope, which erupted at a very small altitude (left column).

The disturbance produced by the impulsively erupting flux rope is represented by the yellow circle. After the passage of this disturbance through loops 1 to 4 they sequentially start moving (Figures 10k–10n). The loops become compressed to each other from below in Figures 10j and 10o.

The outward-propagating disturbance and the involvement of the loops into the expansion is demonstrated in Figure 11, which presents the time history of the CME formation in one-dimensional spatial profiles. The profiles were computed from the running-difference 193 Å images in a fixed direction of $-36°$ southward from the West and averaged over a 10-pixels wide slice. The image in Figure 11 is similar to the slit images presented by Ma *et al.* (2011) in their Figure 3 but shows more details due to a harder image processing.

Any moving feature appears here as an inclined strip, whose instant slope is its velocity. The traces of the four loops 1–4 shown in Figure 10 are clearly visible. Initially the loops rise slowly; in an interval of 05:35:40–05:37:30 their velocities considerably increase, remaining nearly constant afterwards. Note that the running differences only show the leading edge, while the trailing part disappears.

The red curve corresponds to the flux rope. A faint trace is detectable $(15 - 20)''$ below it up to 05:38:30 and, possibly, later. This trace seems to belong to the flux rope, while the lag is partly due to the varying direction of its fastest expansion, mostly different from $-36°$ (see Figures 7f–7k). The presence of this trace in 193 Å (and 131 Å) without any manifestations in 171 or 211 Å indicates a temperature around 17 MK in the detected part of the flux rope (see Figure 1).

A fastest faint trace is detectable in the nearly radial direction after 05:36:10 even inside the forming CME, starting from a height of $\approx$ 95 Mm. Its yellow outline was calculated for the wave propagation using a power-law fit (see Section 2.2; Grechnev *et al.*, 2008b, 2011b, 2014b, 2015) with a wave onset time

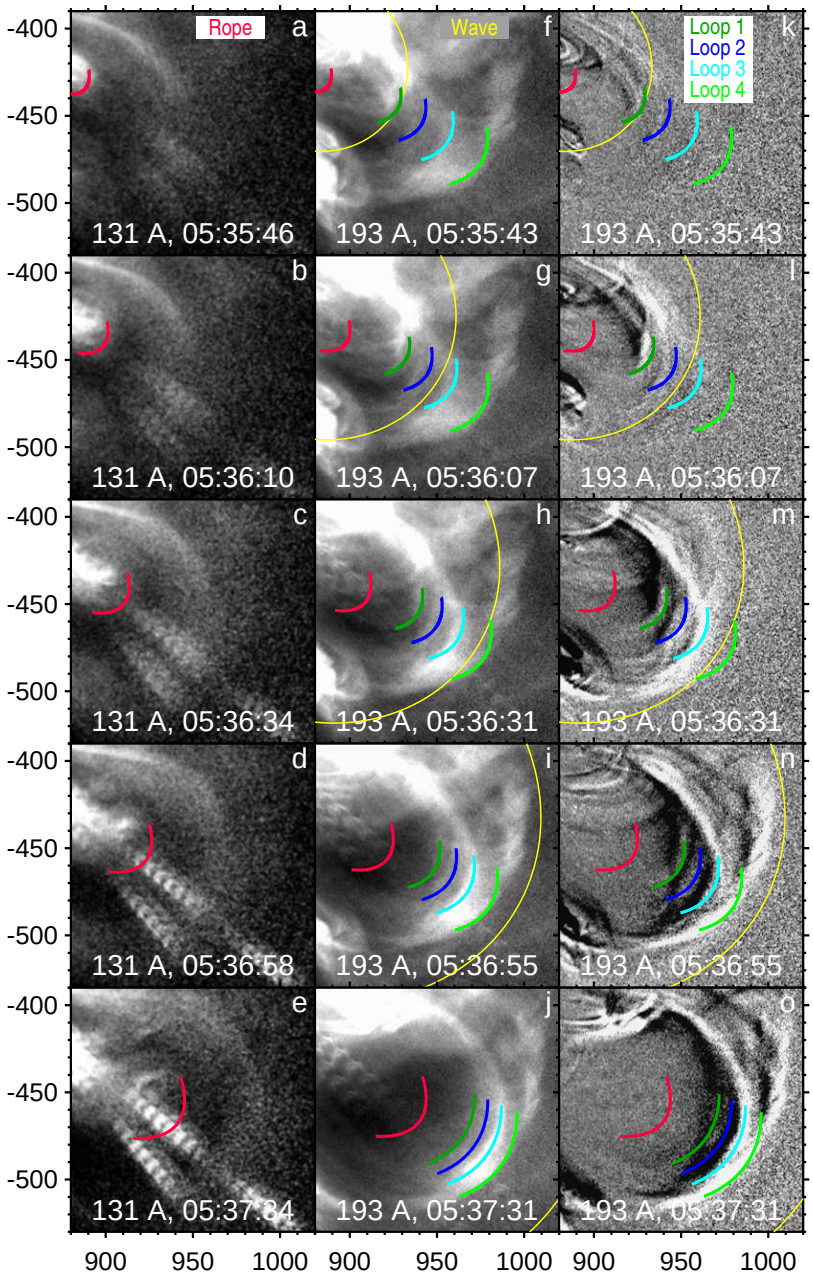

Figure 10. The eruptive flux rope in AIA 131 Å images (left column, a–e) and the loops sequentially involved in the eruption observed in 193 Å (middle and right columns). The middle column (f–j) presents the 193 Å images with a reduced background. The right column (k–o) presents their 12-s running differences. The red arc outlines the top of the eruptive flux rope. The yellow arc outlines the wave. The four other color arcs approximately outline four conspicuous loops 1–4 of a pre-eruption arcade.

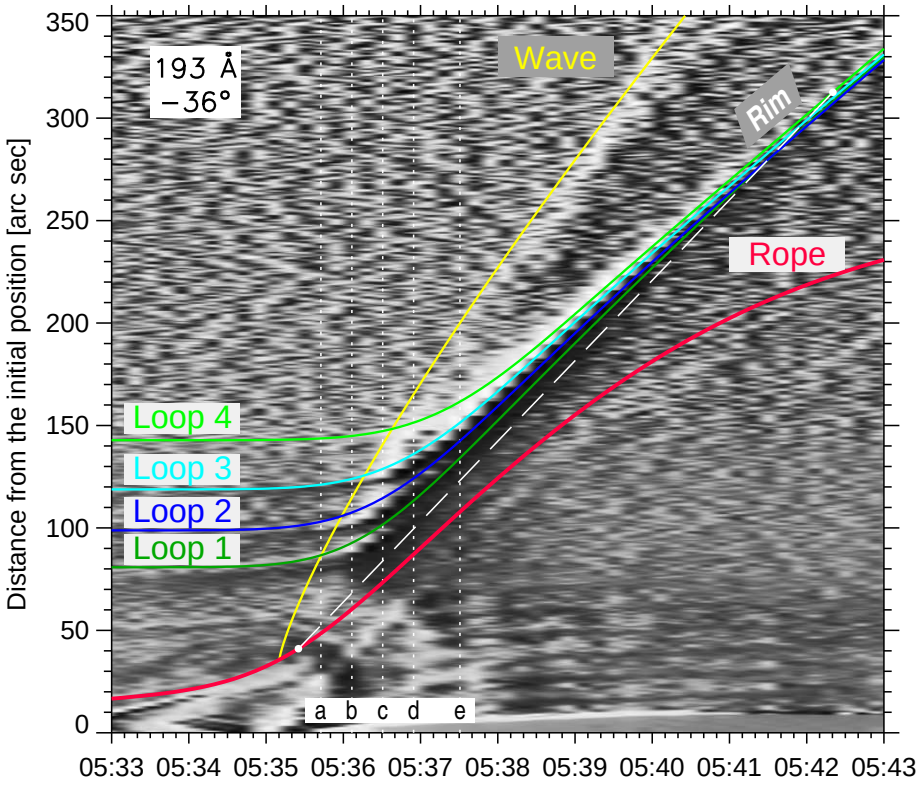

Figure 11. Time history of the CME formation in one-dimensional spatial profiles computed from running-difference 193 Å images in a direction of −36° southward from the West. The red curve represents the flux rope. The yellow curve outlines the trace of the wave. The remaining color curves outline the trajectories of the expanding arcade loops (same colors as in Figure 10). The vertical lines mark the observation times of Figures 10a–10e. The labels of the corresponding panels are indicated at the bottom. The tilted dashed line denotes the trajectory of a virtual piston discussed in Section 7.

corresponding to the flux rope's acceleration peak, t_0 = 05:35:10, and a density falloff exponent $\delta = 2.5$. The yellow ovals in Figure 10 correspond to this fit.

It is possible to figure out the kinematics of loops 1–4 in Figure 11 qualitatively, keeping in mind that the expansion of the loops was limited from above by the rim. Initially the loops were static. The outward-propagating wave reached loops 1, 2, 3, and 4 one after another, and sequentially drove their expansion. Loop 1 acquired a highest speed and then had to decelerate, being restricted by the rim. The highest speeds, accelerations, and decelerations of loops 2, 3, and 4 slightly decreased progressively. The final speeds of the four loops converged to the final speed of the rim.

Four color curves in Figure 11 outline the trajectories of loops 1–4. Parameters of these analytic curves were adjusted to match the traces of the loops. Previously, Eselevich and Eselevich (2013) approximately measured the height–time plots of the rising loops and proposed a fast emergence of a magnetic tube from below the photosphere at about 05:33. This idea contradicts the slow rise

of the CME-progenitor coronal structures during the long-lasting pre-eruption heating and the early onset, by 05:31, of a sharp increase of the 131 Å and 0.5–4 Å emissions (see Figures 7a–7e and Figure 8). Nevertheless, Eselevich and Eselevich (2013) correctly showed in their Figure 7a the sequential involvement of the loops into the motion.

The analytic color height–time plots in Figure 11 allowed us to infer the quantitative kinematics of the loops. The corresponding plots for the four loops, flux rope (red) and wave (dashed yellow-gray) are presented in Figures 12a–12c.

Figure 12a reproduces Figure 11 without the background image. Figure 12b shows the velocity–time plots. The highest velocities reached by the flux rope and the four loops were between 400 and 500 km s^{-1}. Note that the wave speed was actually twice higher than the dashed yellow-gray curve shows, and started from $\gtrsim 1000$ km s^{-1}, which is a typical fast-mode speed in the low corona above an active region. Then the wave speed monotonically decreased all the time.

The flux rope speed was ≈ 250 km s^{-1} at the wave onset time, $t_0 = 05{:}35{:}10$, and rose farther. Loop 4 and the forming rim started to expand well after the wave onset time, and therefore could not excite the wave. The relation between the velocities of the flux rope and wave rules out its bow-shock regime. Also, the velocities of the loops varied gradually, indicating that the wave was not yet in the shock regime until, at least, its passage through loop 4 at 05:36:30 in the direction of the measurements $-36°$ southward from the West. Otherwise, the velocity of a loop pushed by a shock wave should change abruptly.

Figure 12c presents the accelerations of the flux rope and the four loops. All components of the forming CME was obviously driven by the erupting flux rope, whose acceleration pulse led all the others. Loops 1–4 sequentially accelerated ($3 - 4$ km s^{-2}) up to $400 - 500$ km s^{-1}, and then somewhat decelerated, approaching the final speed of the rim. The monotonically decreasing deceleration of the wave is not interesting and not shown.

Figure 12d shows the aspect ratio estimated for the top of the forming CME in manual outlining the curvature of loop 4, which then joined the rim (the black arc in Figure 5 and the green arc in the AIA_131_171_loops.mpg movie). The uncertainty is shown by the shading. Comparison with Figure 12c reveals a similarity between the variations of the aspect ratio and the deceleration of the flux rope. However, attempts to use the deceleration curve in outlining the CME top showed that its curvature (*i.e.*, the aspect ratio) increased slower than the deceleration ceased (*cf.* the shapes of the two curves after 05:40). Thus, the variations in the aspect ratio of the CME bubble were probably governed by the flux rope expanding inside it, while its reaction had a reasonable delay.

It is worth to compare our measurements with the results obtained previously. Patsourakos, Vourlidas, and Stenborg (2010) were the first who measured the speed, acceleration, and the aspect ratio of the rim (CME bubble). They found that its speed reached a maximum of 400 km s^{-1} at 05:38 and then decreased to 300 km s^{-1}. The maximum acceleration of 2 km s^{-2} was found to occur slightly after 05:36, followed by a deceleration up to -0.5 km s^{-2} around 05:39. With quite different measurement techniques used by us and the authors, both results appear to be close to each other with an acceptable accuracy.

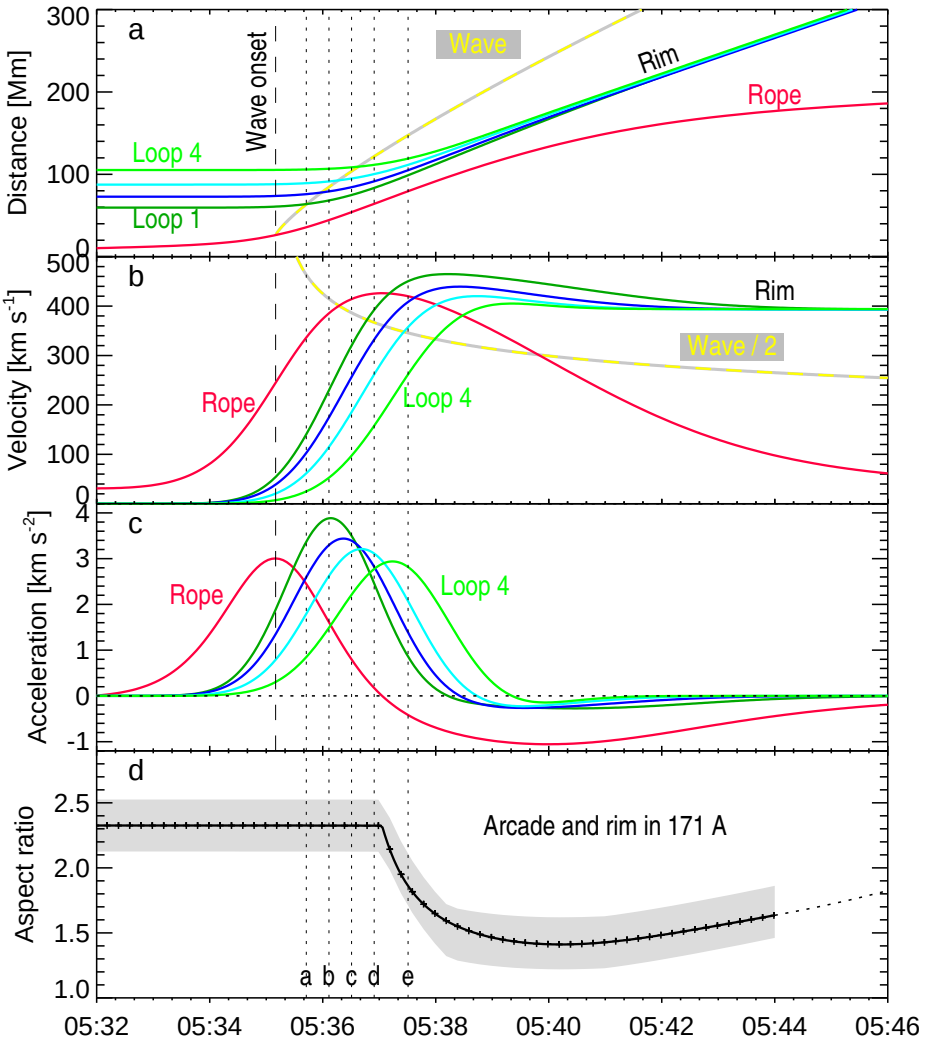

Figure 12. Kinematics of the flux rope, arcade loops 1 – 4, and the wave (same colors as in Figures 10 and 11). (a) Distance–time plots similar to Figure 11. The vertical dotted lines mark the observation times of Figures 10a – 10e. The labels of the corresponding panels are indicated at the bottom. The vertical dashed line marks the wave onset time. (b) Velocity–time plots. The wave velocity (dashed yellow-gray) in the plot is reduced by a factor of 2. (c) Accelerations of the flux rope (red) and arcade loops 1 – 4. (d) The measured aspect ratio of the arcade loop 4 and rim. The shading represents the uncertainty. The dotted extension approximately corresponds to the later expansion, when the rim is not reliably detectable.

The aspect ratio variations we measured are basically close to those found by Patsourakos, Vourlidas, and Stenborg (2010), with somewhat larger differences due to different ways of the measurements. Substantial is the recovery of the aspect ratio after 05:40 which is also indicated by the measurements of Gopalswamy *et al.* (2012) in their Figure 3b. This circumstance implies that the varying aspect ratio, considered by Patsourakos, Vourlidas, and Stenborg (2010)

as a lateral overexpansion of the CME bubble, was a reversible temporary effect, that does not confirm the idea of the authors about its significance for the CME formation process.

Due to the difficulties to detect the earliest signatures of the wave and to measure its kinematics, there is a scatter between the results of different authors. Kozarev *et al.* (2011) found the wave speed of about 735 km s^{-1} at 05:37 and its subsequent deceleration that is very close to our results. Ma *et al.* (2011) presented two versions of the estimates, each with a certain deceleration after 05:40 from 600 km s^{-1} to about 500 km s^{-1} at 05:42–05:44, also mainly consistent with our results.

5.1.2. Rim and Pileup on its Top in 211 Å AIA Images

To study the details of the pileup formation on top of the rim shown in Figure 6, we consider the 211 Å AIA images in a way similar to the preceding Section. Here we use a different direction, in which the loops inside the rim are indistinct, but the rim, pileup, and wave trace are clearly visible. Figure 13a presents a time-history diagram computed from running differences of the 211 Å images in a direction of -22° southward from the West.

The trace of the arcade top represented by loop 4, which joined the rim, is distinct by about 05:40, and later it becomes poorly visible. Nevertheless, comparison of its faint trace with the dashed continuation of the earlier trajectory measured from Figure 11 indicates that the rim starts decelerating.

A much faster wave trace is outlined by the yellow fit. The 211 Å data reveal an additional, slower bright branch outlined by a pink curve. It goes nearly parallel to the trace of the rim, being $\approx 90''$ higher. The high trace corresponds to the white arc in Figure 6 outlining the outer edge of the pileup. In order to relate it to the white-light CME, we calculated the kinematics of the frontal structure using the self-similar approximation (Grechnev *et al.*, 2014b) with the parameters estimated to coordinate the 211 Å AIA and SOHO/LASCO observations. The pink outline was obtained with $V_1 = 380$ km s^{-1} and $r_1 = 264$ km ($360''$) at $t_1 =$ 05:41:00, and $V_\infty = 190$ km s^{-1} (the whole fit is shown in Figure 16 by the solid line). The compression of the loops to the rim indicates that the self-similar approximation did not yet rigorously apply at 05:41:00 (otherwise, the CME should expand uniformly); nevertheless, the pink outline in the distance–time diagram and the velocity-time plot in Figure 13b appear to be acceptable. The only drawback is that we cannot concatenate smoothly the green rim's velocity with the pink CME speed, although they are close to each other.

To understand the pileup formation better and to figure out the properties of the wave, we consider a similar diagram in Figure 14 computed in the same direction from fixed-base difference AIA 211 Å images. It was very difficult to reveal individual structures between the rim and the leading edge, and therefore their separate traces outlined by the black dashed lines are regrettably faint, in spite of our efforts. Several attempts showed that the errors in estimating the slopes of the faint traces in Figure 14a (*i.e.*, their velocities) did not exceed $\pm 7\%$.

Previous studies assumed that the shock came into being before 05:37, when the type II burst started, but we are not certain when the wave entered the shock

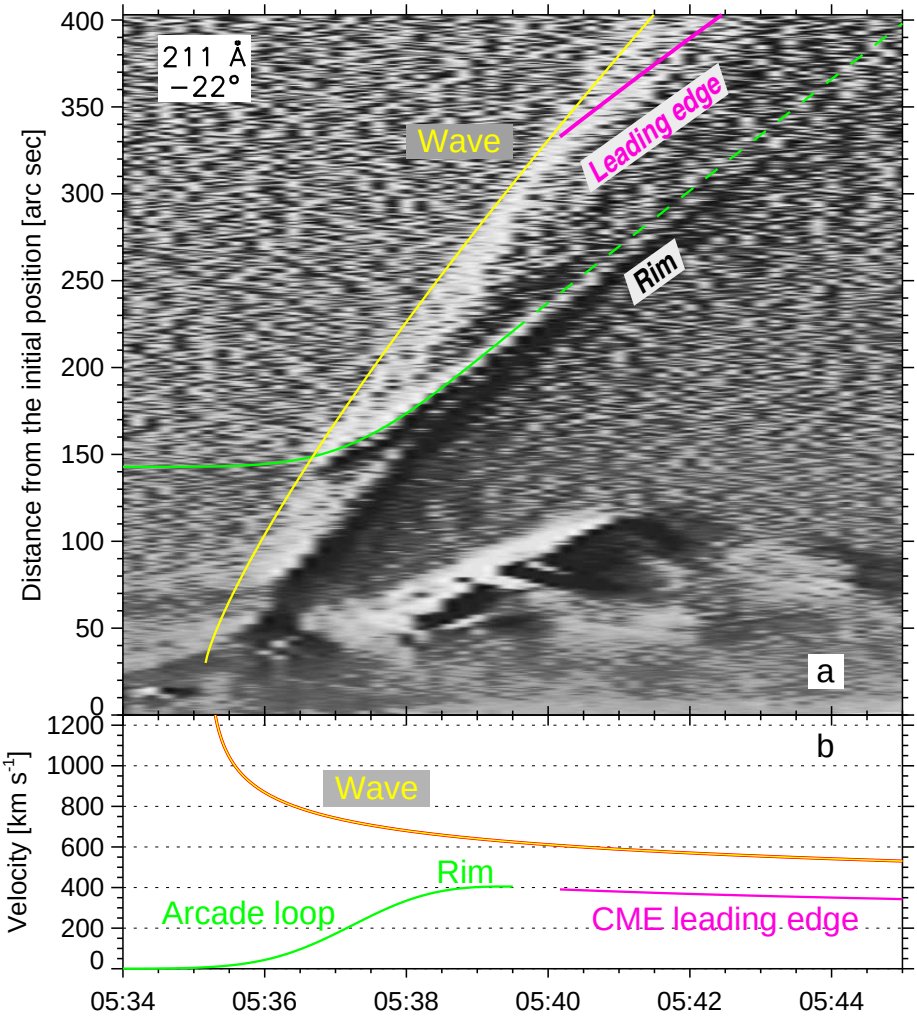

Figure 13. (a) Time history of the CME formation in one-dimensional spatial profiles computed from running-difference AIA 211 Å images in a direction of −22° southward from the West. The yellow curve outlines the wave trace. The green curve corresponds to the arcade top (loop 4) clinging to the rim. The later part of the rim signature shows a stronger deceleration then loop 4 in Figures 11 and 12 (the dashed continuation of the green curve) had. The outermost signature of the bubble is outlined with the pink curve corresponding to the leading edge of the CME frontal structure. (b) Velocity–time plots for the wave (yellow on gray), the upper arcade loop 4 and the rim (green), and the CME leading edge (pink).

regime in the direction of −22° southward from the West. Figure 14 does not allow one to recognize if the transition from the white horizontal dashed lines left from the wave front to the inclined black dashed lines was abrupt (shock) or gradual. It is possible to estimate only the upper limit, $M_{\rm max} = V_{\rm sh}/V_{\rm fast}$, for the actual Mach number, M, so that $1 \le M \le M_{\rm max}$.

With known velocities of the wave front, presumably shock, $V_{\rm sh}$, and a structure moved by the gas behind the shock, $U_{\rm sh}$, one can estimate the fast-mode

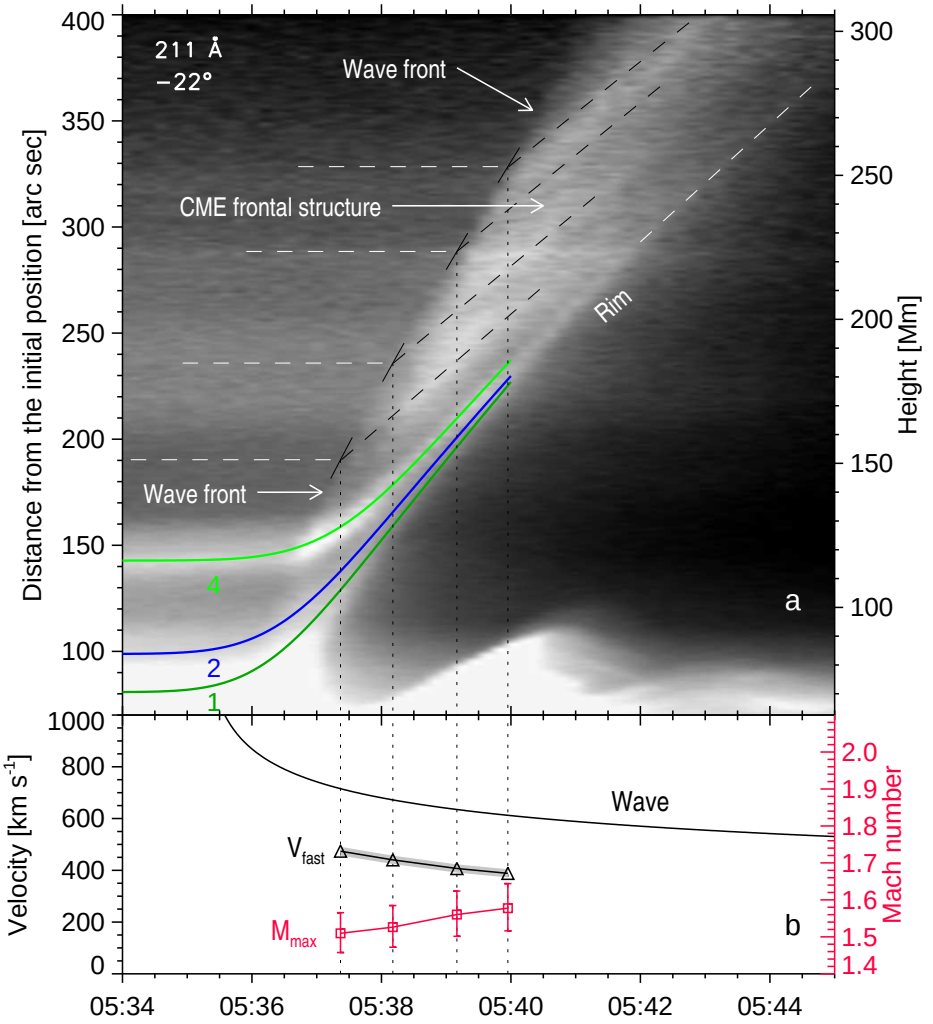

Figure 14. (a) Formation of the CME frontal structure in one-dimensional spatial profiles computed from fixed-base differences of SDO/AIA 211 Å images in a direction of −22° southward from the West. The black dashed lines outline individual structures involved into the motion by the wave, whose front is outlined by the rare dashes. The white horizontal dashed lines left of the wave front denote presumable initial positions of these structures. The color curves labeled 1, 2, and 4 correspond to the loops discussed previously. The right white dashed line outlines the rim. (b) Velocity–time plots for the wave (long black curve), the maximum Mach number (red squares) with uncertainties, and the calculated fast-mode speed (triangles) with uncertainties shown by the shading.

speed, $V_{\rm fast}$, from an equation $V_{\rm sh} \approx V_{\rm fast} + \kappa U_{\rm sh}/2$; the κ coefficient governs the steepening rate of the wave front (Grechnev *et al.*, 2011b). This coefficient, $1/2 \leq \kappa \leq 3/2$, depends on plasma beta and the propagation direction (see diagram in Figure 8 of Afanasyev and Uralov, 2012). Most likely, here we are dealing with a wave propagation nearly perpendicular to the magnetic field in low-beta plasma, $\kappa \approx 3/2$. The estimates of the maximum Mach number and

the fast-mode speed for four instants are shown in Figure 14b. Note that such estimations do not depend on the blast-wave or bow-shock regime, while their accuracy decreases for strong shocks.

As a gradual trajectory of loop 4 in Figure 14a indicates, at 05:36:45 the discontinuity has not yet formed. Figure 14b indicates that the Mach number in the interval from 05:37:25 to 05:40:00 could only increase, not exceeding $M_{\max}$, which was nearly constant, $1.45 \leq M_{\max} \leq 1.65$. The wave probably evolved from a linear fast-mode wave ($M = 1$) to a simple wave and then steepened in some time into the shock with $M < M_{\max}$. It is not excluded that the shock has not formed at all in this direction, just ahead of the CME. The source of the type II burst could be located at a flank of the wave front—*e.g.*, in a small streamer-like structure denoted in Figure 6a.

The fast-mode speed shown in Figure 14b was calculated under an assumption of the weak shock regime of the wave. If this was not the case for all the four instants, then the real fast-mode speed should be between the line connecting the triangles and the higher plot of the wave, anyway decreasing with height. The decrease is typical of the fast-mode speed above active regions at heights $< 0.4R_{\odot}$ (Dulk and McLean, 1978; Gary, 2001; Mann *et al.*, 2003).

In summary, Figures 13 and 14 demonstrate that the formation of the CME occurred due to the outward-propagating wave, which swept up all the structures in its way, involving them into the expansion. The CME frontal structure was mostly constituted by the pileup on top of the expanding rim that previously was a relatively high environment of the active region. Similar conclusions were made by Cheng *et al.* (2011) from the analysis of a different event.

5.2. CME Expansion Visible in White Light

The CME produced in the 13 June 2010 event was observed by SOHO/LASCO. It is important to coordinate our results drawn from the analysis of the eruption observed near the solar surface in EUV with the white-light CME observations. We show some selected LASCO/C2 images in Figure 15. The CME leading edge and wave traces are outlined according to the kinematics presented in Figure 16.

Different representations of the same four images are shown in the upper and middle rows of Figure 15. We endeavor to reveal a poorly visible CME structure in the upper row and to detect faint wave traces in the middle row. The leading edge of the frontal structure (FS) is outlined by the oval arc, whose increasing radius corresponds to the pink self-similar fit in Figure 13. The faintly visible FS seems to consist of stretched loops, while the rim is not pronounced in the CME structure. The CME orientation kept on turning from the initial $-46°$ in Figure 7f to $-16°$ in Figure 15d (position angle of 254° in the CME catalog http://cdaw.gsfc.nasa.gov/CME_list/; Yashiro *et al.*, 2004).

The crosses in the upper and middle rows represent the measurements taken from the CME catalog. They were made for the fastest feature and are close here to the wave traces, which are outlined by the dashed circle. The wave outline is the same as we used in the preceding Section, with $t_0 = 05{:}35{:}10$ and $\delta = 2.5$.

The four later C2 images in the lower row reveal a flux-rope structure of the CME core. The average speed of its center outlined with the dotted circle in

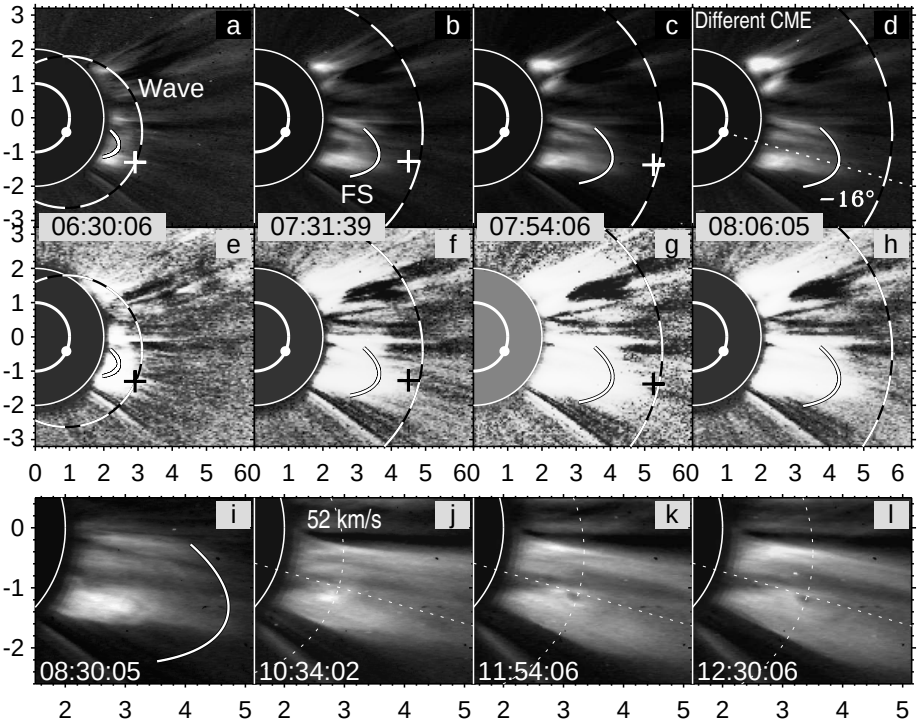

Figure 15. LASCO/C2 images: CME expansion (upper row, fixed ratios), wave traces (middle row, running differences), and the structure of the CME (lower row, fixed ratios). The small oval arcs outline the leading edge of the frontal structure (FS). The larger dashed circles in the upper and middle rows outline the wave traces. The crosses denote the measurements in the CME catalog. The dotted circle in the lower row corresponds to the velocity of the flux rope's center of ≈ 52 km s^{-1}. The thick circle denotes the solar limb. The larger thin circle denotes the inner boundary of the C2 field of view. The small filled circle denotes the eruption site. The axes present the coordinates from the solar disk center in solar radii.

Figures 15j–15l is 52 km s^{-1}, consistent with our measurements in Figure 8c. The flux rope, whose initial expansion drove the whole CME formation process, later relaxed and became the CME core visible well behind its leading edge.

The kinematical evolution of the CME frontal structure and the wave ahead it is clear from Figure 16. The frontal structure was probably formed from coronal loops swept up by the expanding rim, whose velocity is plotted in Figure 16b with the dotted line. Being expelled by the erupting flux rope, the wave initially was fast and possibly strong enough to produce the type II emission within the hatched interval. The wave speed in the radial direction decreased within this interval from ≈ 680 to ≈ 460 km s^{-1}. Note that the type II burst source could be located in a different direction, where the wave strength might be also different.

Then the wave strongly decelerated and dampened, being not driven by the trailing piston, which considerably slowed down. The evolution of the wave speed inferred from AIA and LASCO observations does not confirm the assumption of some authors about its possible peak between $1.5R_\odot$ and the first appearance in the LASCO/C2 field of view at $2.6R_\odot$. Although the kinematics of the wave

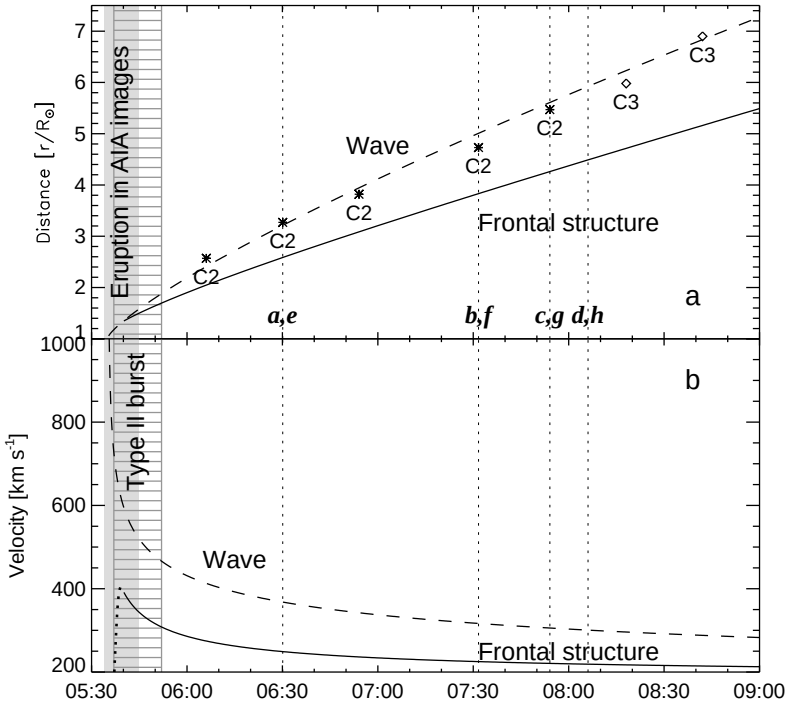

Figure 16. Heliocentric distance–time (a) and velocity–time (b) plots for the leading edge of the CME frontal structure (solid) and the wave (dashed). The symbols in panel (a) represent the measurements from the CME catalog. The vertical dotted lines denote the times of the images in Figure 15. The labels of the corresponding panels are indicated at the bottom of panel (a). The initial accelerating part (dotted) in panel (b) corresponds to the arcade loop and the rim in Figure 13. The gray shading corresponds to the time interval presented in Figure 13. The horizontal hatching denotes the interval, in which the type II burst was observed.

and the CME behind it were similar to each other, the wave speed at distances $> 2R_{\odot}$ was too low for the bow-shock regime. Then the wave speed further decreased at about $7R_{\odot}$ below 300 km s^{-1}, comparable to the solar wind speed, that points to its decay into a weak disturbance. The increasing role of the solar wind is confirmed by the subsequent acceleration of the CME suggested by the measurements in the CME catalog.

6. Wave Signatures and EUV Transient

6.1. EUV Wave

Most authors of the preceding studies considered a transient expanding in EUV images (EUV wave) as a signature of a shock wave, assuming its bow-shock regime. We showed in the preceding Sections that the EUV wave moving away from the Sun consisted of swept-up plasmas on top of the expanding separatrix surface, with which the rim was associated. The pileup was involved into the

motion by the outward-propagating wave, which was initially excited by the impulsive expansion of the flux rope, and then resembled decelerating blast wave.

The propagation conditions along the solar surface are considerably different from those away from the Sun. The wave expanding in the lateral directions is not followed by the separatrix surface to large distances. It is therefore important to study the EUV wave propagating in different directions.

Downs *et al.* (2012) analyzed the EUV wave in this event in realistic coronal conditions on the basis of a sophisticated thermodynamic MHD simulation. The authors stated a clear distinction between the wave and non-wave component and concluded that the propagating EUV transient exhibited the behavior of a fast-mode wave. However, it was difficult to ascertain the wave excitation scenario in this simulation.

On the other hand, our approach allows us to study only the global properties of a propagating wave, without a reference to realistic inhomogeneous conditions in the corona. We will nevertheless try to reconcile the wave excitation scenario revealed in the preceding Sections with a posterior near-surface wave propagation and examine how acceptable its fit in this case works.

The EUV wave was observed from two vantage points by SDO/AIA and by STEREO-A/EUVI in 195 Å. Some latter images are shown in Figure 17. Their nominal observation times are specified in the figure. The kinematical plots, from which the ellipses outlining the wave propagation were calculated, are presented in Figure 18, where the EUVI observation times are referred to the SDO vantage point. The wave kinematics along the spherical solar surface was calculated with the same onset time as previously, $t_0 = 05{:}35{:}10$, and a density falloff exponent of $\delta = 2.1$. The blue ellipses in Figure 17 (yellow in the EUVI_wave.mpg movie) delineate the near-surface isotropic trail of an expanding global wave front. This trail corresponds to an effective height of 35 Mm and the wave propagation in the corona without any inhomogeneities. The ellipses were calculated as small circles at a sphere with a pole coinciding to the eruption center.

The calculated ellipses tolerably correspond to the propagating leading edge of the bright EUV wave in the images, although the initial wave could be actually somewhat faster than the outline. The effective height might not be constant, and a small displacement of the wave 'epicenter' is not excluded. Such a displacement toward a region of a higher fast-mode speed was reported previously indeed (see, *e.g.*, Grechnev *et al.*, 2013). The faintness of the EUV wave in these EUVI images disfavors detection of this effect.

The most probable source of a type II radio burst is the current sheet of a small coronal streamer stressed by a shock front (see Section 6.2). The type II burst in this event started at 05:37:00 (Figure 21). The yellow arrow in the upper row of Figure 17 points at the base of a streamer-like feature visible in the AIA 211 Å image in Figure 6a. The wave front in Figure 17a has already passed this feature, while the observation time of this STEREO-A/EUVI image corresponds to 05:37:31 UT. Thus, the actual positions of the wave front do not contradict a possible location of the type II burst source in this feature.

Figure 19 presents the EUV wave propagation visible in the AIA 211 and 171 Å images. The blue curves outlining the off-limb front were composed from three oval arcs adjusted to fit the kinematics of the wave propagation measured

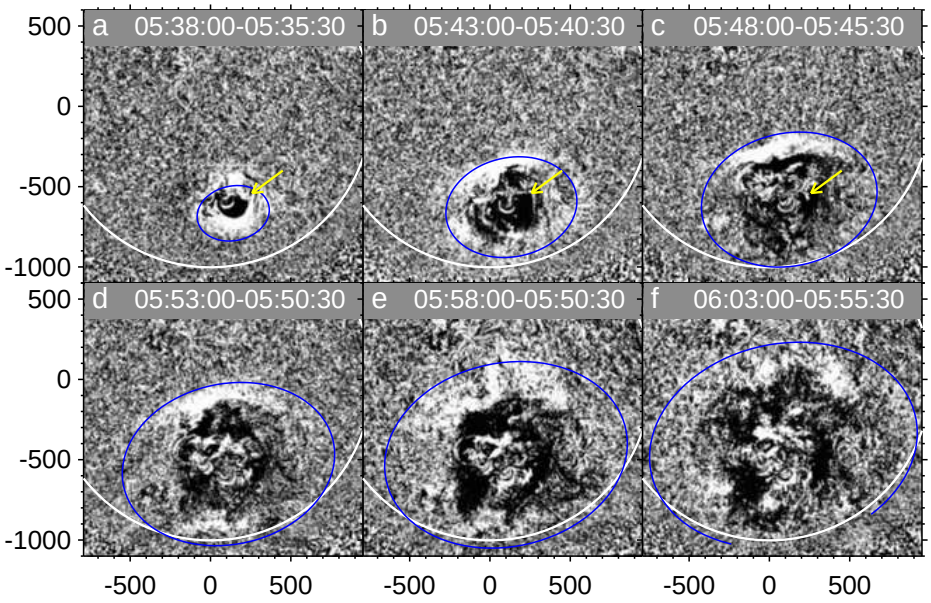

Figure 17. EUV wave propagation in STEREO-A/EUVI 195 Å running difference images. The blue ellipses represent calculated wave fronts. The yellow arrow in panels (a)–(c) points at a base of the streamer-like feature (denoted in Figure 6a), in which the source of the type II burst could be located. The white circles outline the solar limb. The axes show the coordinates in arcsec from the solar disk center.

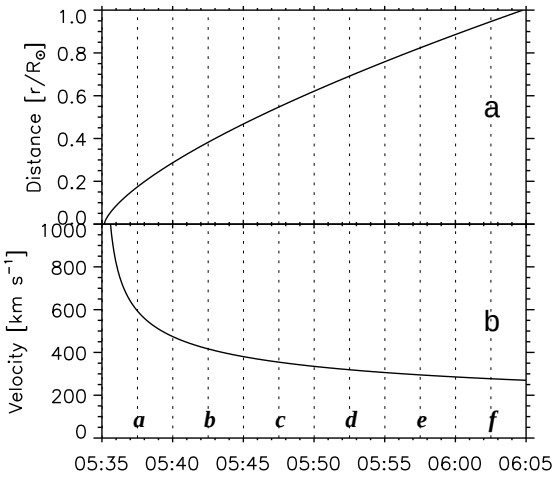

Figure 18. Distance–time (a) and velocity–time (b) plots of the EUV wave propagation along the solar surface. The vertical lines mark the observation times of Figures 17a – 17f corrected for the difference between the orbits of the Earth and STEREO-A, as if the Sun were viewed from SDO. The labels of the corresponding panels are indicated at the bottom.

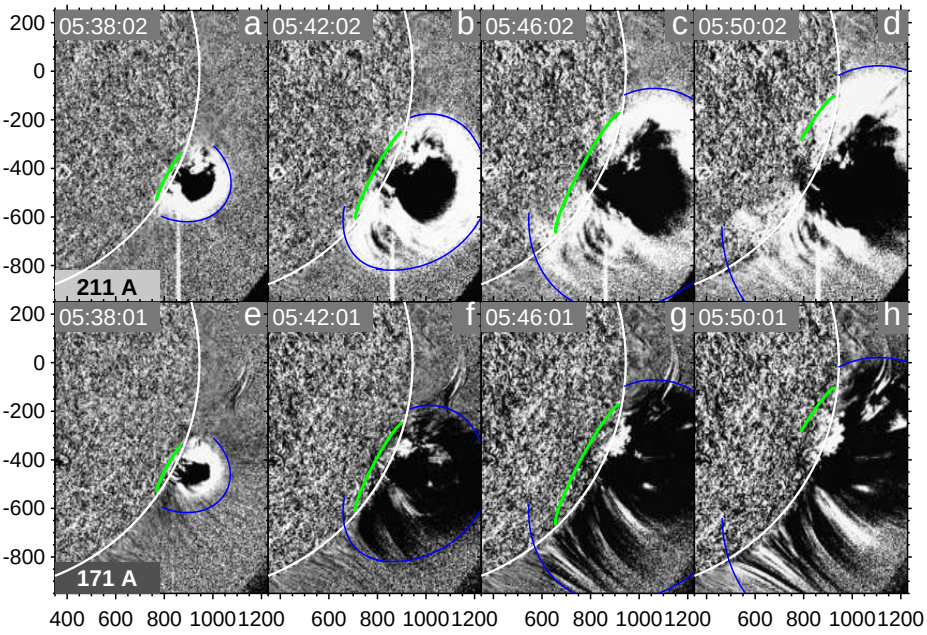

Figure 19. EUV wave propagation in AIA 211 and 171 Å fixed-base image ratios to those at about 05:34:00. The blue curves outline the off-limb wave front. The green ellipses outline its surface trail visible on the Earth-facing hemisphere. Two right panels reveal the wave reflection in the southern region. The white circles denote the solar limb. The axes show the coordinates in arcsec from the solar disk center.

from the quadrature observations with STEREO-A/EUVI and SDO/AIA. The orientations of the north and south arcs were progressively adjusted to catch the tilt of the wave front that apparently varied in its motion along the limb. The radius of the south arc calculated from the power-law fit was stretched by a constant factor to catch the faster wave propagation toward the South Pole, where the fast-mode speed was higher in the region of the polar coronal hole. The green ellipses were calculated for the surface trail of the wave front visible on the Earth-facing hemisphere.

The EUV transient appears between the calculated wave front and the rim as a brightening in the higher-temperature 211 Å images in the upper row and as a darkening in the lower-temperature 171 Å images in the lower row. The brightening in the first 171 Å image in Figure 19e is due to separate loops, which have not yet merged into the thin rim. The EUV transient is most likely due to the pileup, while the different appearance in the two different-temperature channels indicates its heating.

Figure 20 compares the appearance of the EUV transient in the 193 Å and 211 Å images. They show the large difference between the orientations of the rim (along with the arcade loops pressed to the rim) and the long loops above it. This fact corroborates the association of the rim to a separatrix surface.

Comparison of Figures 20a and 20b indicates a larger opacity of the pileup on top of the rim in the higher-temperature 211 Å channel (excluding the hottest

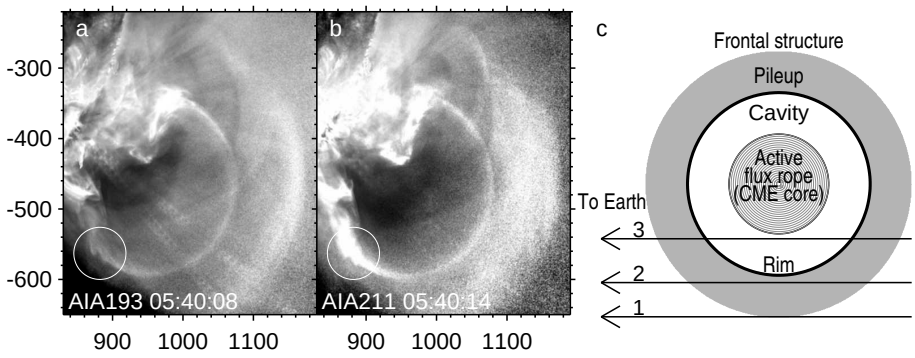

Figure 20. CME bubble in the 193 Å (a) and 211 Å (b) background-subtracted images at the indicated times divided by the images averaged within 05:31:45–05:33:25. The circle outlines the trace of a lateral disturbance, which accompanies the lift-off of the flux rope and runs along the separatrix. The sketch in panel (c) presents the CME bubble as viewed approximately from STEREO-A and illustrates the brightness distribution observed from the near-Earth SDO vantage point.

window in 193 Å) and some temperature increase from the outer edge of the pileup to the rim. The appearance of the pileup suggests that it was a thick, nearly spherical layer, bounded by the rim from inside, as shown in Figure 20c.

6.2. Type II Burst

The type II burst observed in this event was analyzed previously (Kozarev *et al.*, 2011; Ma *et al.*, 2011; Gopalswamy *et al.*, 2012; Vasanth *et al.*, 2014; Kouloumvakos *et al.*, 2014) based on data from different radio spectrographs, each of which has its own advantages and limitations. We have combined a wide-range HiRAS spectrum with higher-resolution spectra recorded at two USAF RSTN stations, Learmonth and San Vito, to enhance their quality. Figure 21b presents the combined spectrum along with higher-sensitivity fixed-frequency data recorded by the Learmonth RSTN radiometers and Nobeyama Radio Polarimeters (NoRP; Torii *et al.*, 1979) at 1 GHz. The pre-burst levels of these time profiles correspond to their frequencies, and their peak fluxes are specified just after the bursts. The bursts correspond to a faint drifting continuum suggested by the HiRAS spectrogram. For comparison Figure 21a shows the acceleration of the flux rope and the HXR burst (similar to Figure 8d). The vertical dashed line denotes the wave onset time, $t_0 = 05{:}35{:}10$.

Dynamic spectra represent a superposition of emissions, which originate generally at different sites. The combined spectrum shows that the type II burst had a complex multi-lane structure, which is difficult to reveal from individual spectrograms. To understand this structure, we have outlined the trajectories of separate lanes with the curves of different line styles and colors. The 'F' subscripts denote the fundamental emission, and 'H' means the harmonic. All of the curves have the same onset time, t_0, and correspond to a single shock front crossing various coronal structures located in different directions relative to the wave origin. The different curvatures of the trajectories are most likely due to different plasma density falloffs, δ, in the corresponding directions.

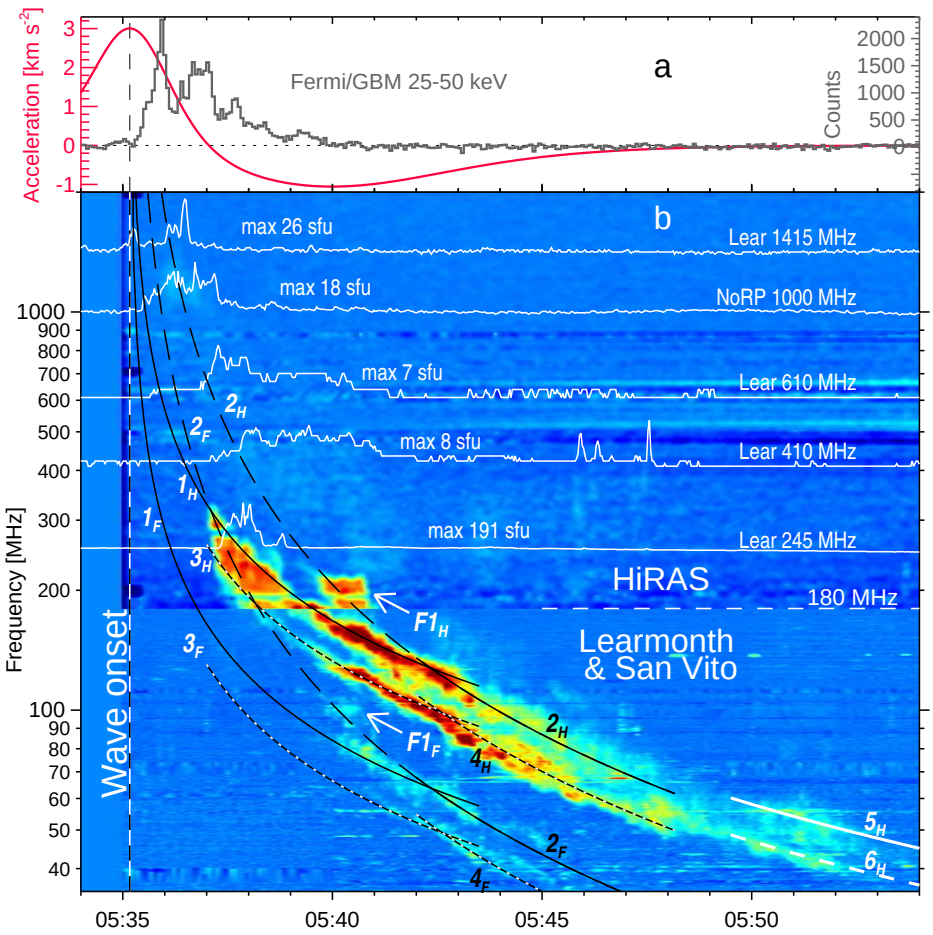

Figure 21. The relation between the eruption, HXR burst, and radio signatures of the propagating shock wave. (a) Acceleration of the flux rope (red) and the HXR burst (gray). The vertical dashed line marks the wave onset time. (b) A dynamic spectrum of the type II burst composed from the HiRAS data (> 180 MHz) and Learmonth and San Vito RSTN data (< 180 MHz) along with normalized fixed-frequency time profiles (Learmonth). The zero levels of the fixed-frequency data correspond to their frequencies in the figure. The peak fluxes of the bursts are indicated. The harmonically related pairs of the type II bands are outlined by the calculated trajectories (1_F, 1_H), (2_F, 2_H), *etc.* of different line styles. An additional harmonic feature $F1_F$, $F1_H$ is indicated by the arrows.

The fixed-frequency data reveal the early wave signatures before the onset of the type II burst. The outlining curves correspond to the onset or rise of the bursts at fixed frequencies, if the radiometers were sensitive enough to detect their fluxes, all of which did not exceed 30 sfu, being < 10 sfu below 700 MHz. The type II burst started at 05:37:00, when the wave front has already passed through the rim and expanded outside farther. The harmonic type II emission was much stronger than the preceding drifting continuum and reached 191 sfu.

The initial trajectories of the paired type II bands 1 and 3 are outlined with density falloff exponents of $\delta_1 = \delta_3 = 2.05$, which are close to that found for the

propagation of a spherical wave along the solar surface ($\delta = 2.1$, Section 6). The fundamental emission is visible only occasionally. Then the bands had turns, which the outlining curves emphasize. At 05:43:00, bands 1 and 3 passed into bands 2 and 4, respectively ($\delta_2 = \delta_4 = 2.58$). Another turn occurred between 05:48:00 and 05:49:30 from harmonic bands $2_{\rm H}$ and $4_{\rm H}$ to bands $5_{\rm H}$ and $6_{\rm H}$, respectively ($\delta_5 = \delta_6 = 2.75$), while the corresponding fundamental bands left the observed frequency range. The bands before the turns and after them overlap.

The $\delta = 2.58$ is not much different from $\delta = 2.5$ found in Section 5 for the wave propagation away from the Sun, being close to the low-latitude Saito model (Saito, 1970; see also Grechnev *et al.*, 2011b). A nearly radial direction is also appropriate for $\delta = 2.75$, corresponding to the Saito model at a higher latitude.

These facts suggest that the type II emission originated initially at a lower-latitude flank of the wave front and then possibly at both flanks, while the sources moved away from the Sun. A number of studies converge to the idea that a probable source of a type II burst is the current sheet of a small coronal streamer stressed by a shock front. This causes a flare-like process running along the streamer (*e.g.*, Uralova and Uralov, 1994; Reiner *et al.*, 2003; Mancuso and Raymond, 2004). A large-scale shock front crossing a wide range of plasma densities in the corona can only produce a drifting continuum (Knock and Cairns, 2005), whereas the radio source located in a distinct extended narrow structure like a coronal ray ensures the narrow-band harmonic emission. This scenario accounted for some structural features of type II bursts observed in different events (Grechnev *et al.*, 2011b, 2011a, 2014b, 2015). Further support to this scenario is provided by the imaging meter-wave observations of type II sources presented by Feng *et al.* (2013), Chen *et al.* (2014), and Du *et al.* (2014).

The split bands 1–2–5 and 3–4–6, which are better visible in the harmonic emission (H) in Figure 21, were previously interpreted in terms of the emissions upstream and downstream of the shock front (Smerd, Sheridan, and Stewart, 1974). The dynamic spectrum shows an additional harmonically related equidistant feature ($\rm F1_F$, $\rm F1_H$), which resembles the split bands in the slope at that time. However, the traditional interpretation cannot account for a third paired band. Du *et al.* (2014) presented observations of type II bursts that also were challenging to this interpretation. Grechnev *et al.* (2011b, 2015) proposed that the band-split type II bursts could be due to emissions from two nearby streamers and supported this option by the observations. The complex structure of the type II burst in this event could be due to both scenarios. The Smerd, Sheridan, and Stewart (1974) interpretation might correspond to the paired bands 1–2–5 and 3–4–6, and not to the ($\rm F1_F$, $\rm F1_H$) feature.

The results of this Section quantitatively agree with the wave development revealed in Sections 5 and 6 and show that some of the considerations and conclusions of the preceding studies need refinement. Relating the type II emission source to the region ahead of the CME nose, invoking the bow-shock properties for the estimations of coronal parameters on the way of the wave front, the assumption of its cylindrical geometry, and some others are among them.

7. Discussion

The 13 June 2010 event presents a rare case when the measurements of the kinematics for the features detectable inside the developing CME allows one to figure out the formation of its structure. The initiator of the event was a solar eruptive filament, whose initial size was small. The outcome of the eruption was the appearance of an expanding coronal wave, whose front resembled a semi-sphere, with a spheroidal cavity inside bounded by a rim. From the observational point of view, our event was strikingly similar to the 23 December 1996 event addressed by Dere *et al.* (1997), who demonstrated for the first time the development of a large-scale CME from a small volume. However, in the 13 June 2010 event, the active role of the eruptive filament located inside the cavity was underestimated.

This underestimation was probably a major reason for the interpretation of this event in terms of a popular concept, in which the coronal cavity plays a major role in excitation of the coronal wave and creation of the CME itself. This concept considers the cavity as a cross-section of a large, single magnetic flux rope, which is a major driver of a CME. The filament (prominence) is regarded as a passive element embedded into the structure of the large flux rope. The filament eruption is considered, at most, as a destabilizing factor triggering the large flux rope. This view is popular, despite the well-known fact that filaments erupting from active regions resemble small filament-associated flux ropes, whose observed behavior does not depend of their large-scale environment. The filaments expand during the acceleration stage earlier and sharper than other structures, and their shapes can rapidly change, according to their small sizes. The impression of the dominant role of a large flux rope, most likely illusive, probably appeared due to relatively slow eruptions of extended filaments outside of active regions, as discussed by Grechnev *et al.* (2015, Section 4.1).

Note that the traditional concept of a magnetic flux rope rooted in the photosphere only by two its ends is a simplification of the magnetic structure of observed solar filaments. A real filament has additional lateral connections to the photosphere by numerous threads. It is therefore not clear what is the surface of the magnetic rope related to a real solar filament. Obviously, this surface may not extend beyond the magnetic domain enclosing the pre-eruption filament. The same is also valid for the coronal cavity, whose boundary is identified with the surface of a magnetic rope. The coronal cavity in the 13 June 2010 event was, most likely, bounded by the magnetic domain containing the pre-eruption filament. This is manifested particularly in the constancy of the photospheric base of the appearing cavity; the cavity remains enclosed by the upward-expanding loops, whose footpoints remain fixed, and the photospheric base does not move along the solar surface. We use henceforth the traditional term 'large flux rope' relating it to the magnetic domain containing the filament.

In the concept of the large flux rope, the only source of a coronal wave is its outer surface, which acts as an expanding piston. In the 13 June 2010 event, this surface was related to the rim. Just due to the appearance of the rim, the development of a presumably piston-driven coronal wave was associated in previous studies of this event. A popular supplement of this concept is an assumption that the wave only enters the shock regime, if the cavity (rim) expands with a

super-Alfvénic speed. The general concept of the piston-driven wave transforms into the bow-shock concept in this way.

7.1. What Was the Driver of the CME and Coronal Wave?

There are two options: either the cavity-associated large flux rope, or the filament-associated small rope inside the cavity. The two concepts seem to be very similar; each of them contains a piston exciting the wave, which can be regarded as a piston-driven one in either concept, as long as the piston influences the wave significantly. A basic question related to the essence of the CME initiation is what played the role of the piston at different stages of the event. In other words, it should be understood if the surface of the piston was inside the cavity or at its boundary, and if the transition between the two regimes was possible.

The adequacy of the concept, in which the large flux rope dominates, does not seem to be justified in our event for the following reasons. The primary driver of any motions in the event was a small eruptive filament located deep within the magnetic core of the active region. The transmission of the motions from the filament outward was obviously wavelike, being easily followed: i) in Figure 12, which shows a sequence of the acceleration and velocity plots for the filament and structures above it, ii) in Figure 10, which shows the temporal relations between the displacements of these structures and pressing them to each other, and iii) in Figure 11, which presents items i) and ii) in a single diagram. The wave front appears in Figure 11 conspicuously earlier than the rim does, but not *vice versa*, as the cavity-dominating concept required. The appearance of the rim is preceded by the compression of magnetic structures located inside the future cavity bounded by the rim rather than outside it. The formation of the rim in Figure 11 appears as the approach of the trajectories corresponding to plasma structures 1–4, which started expanding after the passage of the wave front. The earlier a structure started to move, the earlier it disappeared in Figure 10 because of a rapid decrease of the emission measure in expanding magnetic loops. Eventually, the rim becomes the outer envelope of magnetic loops, whose behavior was similar to each other.

The trajectory of the wave front in Figure 11 originates at the trajectory 'Rope' corresponding to the top of the eruptive filament, which transformed into a bundle of hot loops. Later it decelerated, whereas the wave trajectory did not respond to this kinematical change. This behavior reflects transferring the role of the piston from the eruptive filament to the forming rim. By connecting the trajectories of the filament-related rope and the rim with a single line corresponding to the so-called virtual piston, we get a solution of a known single-piston problem (see, *e.g.*, Sedov, 1981). The trajectories of the wave front and virtual piston intersect, when the piston was the filament-associated rope. Hence, the primary source of the wave was the filament-associated rope inside the cavity rather than its outer boundary (rim).

In summary, the role of the major piston responsible for the wave excitation and formation of the rim was played by the small expanding filament-associated rope, which occupied the central part of the cavity. This is clearly shown by the CME formation. As time elapsed, this piston dilated, acquiring a clinging

magnetic shell, and the whole volume of the cavity became the virtual piston, whose surface became the rim. This scenario seems to present consensus between the two different concepts.

We do not consider the wave excitation scenario by the flare pressure pulse. In a solar flare occurring due to magnetic reconnection, it does not seem possible to produce the plasma pressure considerably exceeding the magnetic pressure. For this reason, the increase in the volume of flare loops is insufficient to produce an appreciable MHD disturbance outward (see Grechnev *et al.*, 2006b, 2011b, 2014b, 2015 for more detail). The plasma density and temperature in flare loops are manifested in their SXR emission. It is intrinsically gradual, resembling the antiderivative of the HXR burst (the Neupert effect; Neupert, 1968), which roughly corresponds to the acceleration of an eruption responsible for a strong MHD disturbance. As Figures 8c and 8d show, the flare in this event has not yet developed, when the wave appeared.

7.2. What Was the Rim?

Two observational facts indicate a close association between the rim and a separatrix surface bounding the magnetic domain, in which the pre-eruption filament resided. i) There is a visible shear between magnetic structures inside the rim and outside it (Section 3.2). ii) The size of the photospheric base of the cavity does not change in the course of eruption.

There are additional important indications. iii) Among the loops visible in two dimensions (2-D) in the AIA_131_171_loops.mpg movie, their envelope only has coincided to the boundary of the cavity. This situation reflects the fact that in the 3-D geometry, the outer envelope of magnetic loops belonging to a single domain is its separatrix surface. iv) A turbulence-like wave trail is expected running along the separatrix surface, following the rising spheroidal cavity. The wave trail should appear due to plasma motions in 3-D magnetic loops belonging to adjacent magnetic domains. These structures should deviate aside and back, as shown in the scheme in Figure 22. Such a trail running along the rim is really visible in Figure 20 (circled) and, especially, in the running-difference AIA_131_211_dist.mpg movie (the asymmetric arc in the movie connects the top of the eruption with the trails on both sides). The trail running along the south part of the rim is indicated by the arrow; the trail running along its north part produces an impression of turbulence. These features altogether reinforce the impression of the oblate shape of the rim.

Intriguing was the conclusion of Patsourakos, Vourlidas, and Stenborg (2010) that 'the lateral overexpansion may well be the process through which eruptions starting small in the corona become large-scale CMEs further out'. However, this observed feature does not seem to be a physically significant factor for the CME formation for the following reasons.

i) As shown in Section 5.1, the decrease of the aspect ratio in Figure 12d, characterizing the apparent ellipticity of the rim, was a reversible temporary effect. One of its causes could be a dampened twisting rotation and writhe of the erupting filament-related rope inside the cavity. Indeed, the liftoff direction of the erupting filament-associated rope rapidly turned during the temporary decrease in the aspect ratio (see Section 4.1).

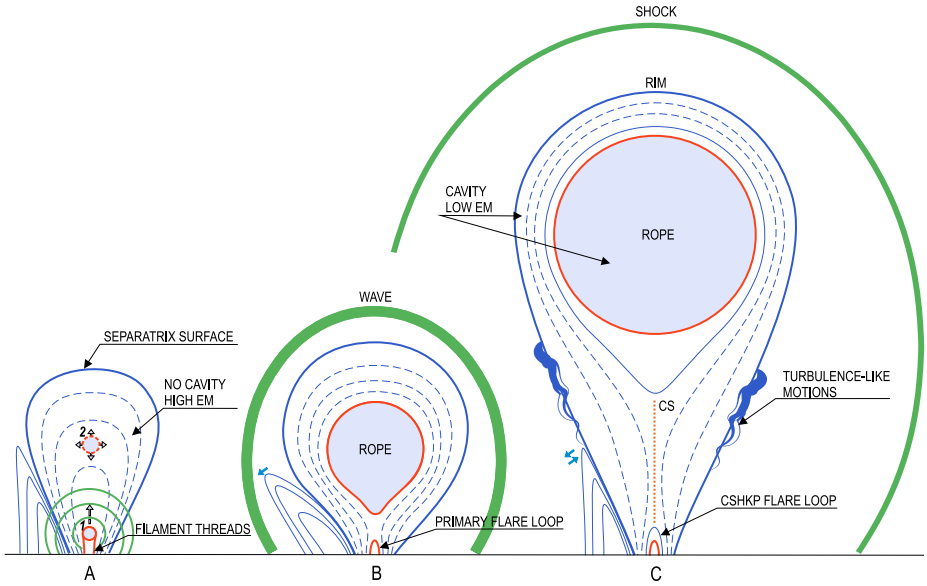

Figure 22. A presumable scenario of the observed event, in which the major driver of the flare, coronal wave, cavity, rim, and CME was a small eruptive filament-associated rope. The cartoon presents a cross section of the active region. The thin blue solid and dotted lines are magnetic field lines. The thick blue line is a separatrix bounding the major magnetic domain. (A) The red circle below is a rope-like structure anchored in the photosphere by its lateral threads. (B) Magnetic reconnection between the filament threads creates a primary flare loop (red). Then the flare proceeds according to the CSHKP model. The motion of the filament-associated rope (red circle) is presented by two steps; first rise, then expansion. A lot of such steps occur. An elementary wave (green ovals in panel (A) corresponds to each step. The front of the resulting disturbance can be a shock discontinuity (green oval in panel (C). The expansion of the magnetic loops between the rope and separatrix is accompanied by the decrease of their visibility. The major magnetic domain transforms into a cavity, whose boundary is visible as a rim. The blue arrows show the deviations of magnetic loops. A sequence of such deviations propagates along the separatrix in the form of a turbulence-like trail.

ii) The apparent ellipticity of the cavity in the 13 June 2010 event might be due to its observed geometry with some extent inclined to the line of sight (see Section 3). Note that the cavity in the analog of our event presented by Dere *et al.* (1997) was perfectly spherical in their Figure 2.

iii) One might relate the increasing ellipticity of the cavity to the bow-shock regime, when the dynamic pressure on the frontal part of the body is important. However, the bow-shock regime is ruled out by the dissimilar evolutions of the wave and rim (CME) speeds in Figure 13b.

7.3. Overall Scheme

Figure 22 summarizes the results of our analysis of the 13 June 2010 event, starting from the onset of the eruption, and does not consider the initiation phase with a long-lasting filament heating. A new key item of this scheme is a dominant, rather than passive, role of a small filament in the formation of the classical structural CME components. These are the coronal cavity, the rim with

the frontal structure, and the coronal wave. The filament associated with a core of this configuration determines the subsequent evolution of all its components.

Figure 22 presents a vertical cross-section of the active region's magnetic core. The base corresponds to the photosphere. The thin solid and dashed lines represent the magnetic field lines. The thick blue line is a separatrix bounding the major magnetic domain. Figure 22A presents in the lower part of the magnetic domain a pre-eruption filament 1 (small red circle), which is a rope-like structure rooted in the photosphere by its lateral threads (red). There is no visible cavity in the initial state; the plasma emission measure in the major domain is rather high. The electric current flowing along the separatrix surface is insignificant. Magnetic loops of an adjacent domain are shown on the left.

Magnetic reconnection of the filament threads creates a primary flare loop (red in Figures 22B and 22C) and primary ribbons, heats the filament, and transforms it into a flux rope (contoured by the red line), which has no lateral connections to the photosphere. Then the flare develops according to the standard CSHKP model.

The expansion and lift-off of the flux rope is shown in Figures 22A and 22B in two stages. Firstly the flux rope (1) rises, keeping its size and a large internal magnetic pressure. Then the rope (2) expands, equalizing internal and external pressure. The lift-off of the rope consists of a multitude of such steps. The deformations corresponding to each step transfer outward by fast MHD waves (green ovals in Figure 22A). Each following wave overtakes a preceding one. The front of a resulting disturbance can become a shock discontinuity (green oval in Figure 22C).

The expansion and stretch of the magnetic loops surrounding the rope (the loops are represented by the blue dashed lines between the red circle and thick blue separatrix) is accompanied by their pressing to each other and a decrease in their emission measure. The loops sequentially disappear. The major magnetic domain transforms into a cavity bounded by the separatrix surface, which is observed as the rim. Its vicinity is, in fact, a moving current sheet separating magnetic field lines of a different connectivity. The current sheet can heat the surrounding plasma. The blue arrows in the left parts of Figures 22B and 22C indicate the deviations of magnetic loops during the passage of the spheroidal cavity that results in the propagation of a turbulence-like trail along the separatrix.

Our consideration finishes here. A subsequent story of CMEs and related waves seems to be more or less clear. Our view, expectations, and results can be found, *e.g.*, in Grechnev *et al.* (2011b, 2013, 2014b, 2015). The CME should enter the stage of a free expansion, which is known to be close to self-similar, *i.e.*, the distances between all of the CME structural components should progressively increase. Most likely, the free expansion regime of the 13 June 2010 CME has not yet established within the AIA field of view. Later on, the loops, which disappeared, apparently merging to the rim, should reappear and diverge in the self-similar regime. The expectations are consistent with the LASCO observations of the CME discussed in Section 5.2. For an independent verification of our conclusions related to the waves, see, *e.g.*, the studies by Kwon *et al.* (2013); Kwon, Zhang, and Olmedo (2014); Kwon, Zhang, and Vourlidas (2015), and others mentioned in the text.

8. Conclusion

Taking advantage of the detailed multi-instrument observations of the 13 June 2010 event with an unprecedented temporal and spectral coverage, primarily thanks to the SDO/AIA data, it has become possible to reveal a consistent picture of a solar eruption, coordinating qualitatively and quantitatively its various observational aspects. The inferred scenario updates and specifies existing hypotheses. Unlike traditional expectations, the major driver of the flare, CME formation, and large-scale wave was the eruptive filament. It heated up to 10 MK and even more; being a direct progenitor of a hypothesized flux rope, just the filament transformed into a bundle of erupting loops, which sharply expanded and thus produced a strong MHD disturbance inside the future CME. This outward-propagating disturbance passed through the forming CME and ran ahead of all its structures. Probably, the disturbance rapidly steepened into a shock resembling a blast wave, produced a type II burst and EUV wave. The magnetic domain containing the eruptive filament – flux rope was forced to expand from inside and became the CME cavity bounded by a separatrix surface observed as a rim, while the enhanced-temperature coronal loops above it were swept up by the expanding rim and became the CME frontal structure.

Although the expected identity of the cavity with a flux-rope has not been confirmed, the role of its rim was important. Being not permeable for plasma, the expanding separatrix surface associated to the rim was responsible for the appearance of a coronal dimming and takes a role of the piston after the deceleration of the flux rope. If the CME were fast, then the wave ahead it eventually changed to the bow-shock regime and became the CME-driven shock in a correct sense. However, this has not happened, because the CME was slow. Instead, the decelerating wave dampened and decayed into a weak disturbance.

In spite of a similarity between the extremities of the bow-shock and blast-wave regimes, some of their properties are different. In particular, when the blast wave is getting weaker, then the distance between its front and the piston decreases, whereas the situation is opposite in the bow-shock regime. For this reason, assumptions of the bow-shock properties for the waves impulsively excited by eruptions might result in an incorrect outcome.

The preceding studies of the 13 June 2010 eruptive event have revealed its important aspects. However, the flux rope, which was a key item of the eruptive process, escaped detection. Due to this drawback, the researchers had to invoke some traditional assumptions, not all of which have been confirmed. It was also very difficult to detect the flux rope for us. It has become possible, because our persistent search was guided by the expectations based on our preceding results (*e.g.*, Grechnev *et al.*, 2011b, 2014a, 2014b, 2015), and in this way we elaborated the data processing and analysis techniques outlined in Section 2. These techniques might also be helpful in different studies.

Most likely, the updated scenario of an eruptive event presented here is rather typical. Incorporating its items into theoretical considerations and numerical simulations seems to be promising for a better understanding solar eruptive phenomena. However, we did not analyze the long-lasting heating the pre-eruptive filament during the initiation stage. This phenomenon was firstly stated by

Zhang *et al.* (2001) and seems to be rather common, being shown explicitly or implicitly, *e.g.*, by Kundu *et al.* (2009), Meshalkina *et al.* (2009), and Grechnev *et al.* (2014a, 2015). Observational and theoretical studies of the causes and mechanisms of this heating could help in perceiving the triggers of solar eruptions and their practical forecasting.

Acknowledgements We thank S.A. Anfinogentov, N.S. Meshalkina, and M.V. Eselevich for their assistance in data handling. We are indebted to A. Kouloumvakos with co-authors and M.A. Livshits for useful discussions. We are grateful to the instrumental teams operating AIA and HMI on SDO, STEREO/SECCHI, Fermi, SOHO/LASCO (ESA & NASA), Nobeyama Solar Facilities, NICT, USAF RSTN network, and GOES satellites for the data used here. We thank the team maintaining the CME Catalog at the CDAW Data Center by NASA and the Catholic University of America in cooperation with the Naval Research Laboratory. This study was supported by the Integration Project of RAS SD No. 4, the Program of basic research of the RAS Presidium No. 9, and the Russian Foundation of Basic Research under grants 15-02-01077, 15-02-01089, and 15-32-20504-mol-a-ved.

References

Afanasyev, A.N., Uralov, A.M.: 2012, *Solar Phys.* **280**, 561. DOI: 10.1007/s11207-012-0022-9

Afanasyev, A.N., Uralov, A.M., Grechnev, V.V.: 2013, *Astron. Rep.*, **57**, 594. DOI: 10.1134/S1063772913080015

Alissandrakis, C.E., Kochanov, A.A., Patsourakos, S., Altyntsev, A.T., Lesovoi, S.V., Lesovoya, N.N.: 2013, *Publ. Astron. Soc. Japan* **65**, SP1, S8. DOI: 10.1093/pasj/65.sp1.S8

Anzer, U.: 1978, *Solar Phys.* **57**, 111. DOI: 10.1007/BF00152048

Asai, A., Yokoyama, T., Shimojo, M., Masuda, S., Kurokawa, H., Shibata, K.: 2004, *Astrophys. J.* **611**, 557. DOI: 10.1086/422159

van Ballegooijen, A.A., Martens, P.C.H.: 1989, *Astrophys. J.* **343**, 971. DOI: 10.1086/167766

Boerner, P., Edwards, C., Lemen, J., Rausch, A., Schrijver, C., Shine, R., Shing, L., Stern, R., Tarbell, T., Title, A. *et al.*: 2012, *Solar Phys.* **275**, 41. DOI: 10.1007/s11207-011-9804-8

Brueckner, G.E., Howard, R.A., Koomen, M.J., Korendyke, C.M., Michels, D.J., Moses, J.D., Socker, D.G., Dere, K.P., Lamy, P.L., Llebaria, A., *et al.*: 1995, *Solar Phys.* **162**, 357. DOI: 10.1007/BF00733434

Carmichael, H.: 1964, *Proc. of AAS-NASA Symp. on the Physics of Solar Flares*, W. N. Hess, **NASA-SP 50**, 451.

Chen, J.: 1989, *Astrophys. J.* **338**, 453. DOI: 10.1086/167211

Chen, J.: 1996, *J. Geophys. Res.* **1012**, 27499. DOI: 10.1029/96JA02644

Chen, Y., Du, G., Feng, L., Feng, S., Kong, X., Guo, F., Wang, B., Li, G.: 2014, *Astrophys. J.* **787**, 59. DOI: 10.1088/0004-637X/787/1/59

Cheng, X., Zhang, J., Liu, Y., Ding, M.D.: 2011, *Astrophys. J. Lett.***732**, L25. DOI: 10.1088/2041-8205/732/2/L25

Dere, K.P., Brueckner, G.E., Howard, R.A., Koomen, M.J., Korendyke, C.M., Kreplin, R.W., Michels, D.J., Moses, J.D., Moulton, N.E., Socker, D.G., *et al.*: 1997, *Solar Phys.* **175**, 601. DOI: 10.1023/A:1004907307376

Downs, C., Roussev, I.I., van der Holst, B., Lugaz, N., Sokolov, I.V.: 2012, *Astrophys. J.* **750**, 134. DOI: 10.1088/0004-637X/750/2/134

Du, G., Chen, Y., Lv, M., Kong, X., Feng, S., Guo, F., Li, G.: 2014, *Astrophys. J. Lett.* **793**, L39. DOI: 10.1088/2041-8205/793/2/L39

Dulk, G.A., McLean, D.J.: 1978, *Solar Phys.* **57**, 279. DOI: 10.1007/BF00160102

Eselevich, V., Eselevich, M.: 2012, *Astrophys. J.* **761**, 68. DOI: 10.1088/0004-637X/761/1/68

Eselevich, V.G., Eselevich, M.V.: 2013, *Astronomy Reports* **57**, 860. DOI: 10.1134/S1063772913110012

Feng, S.W., Chen, Y., Kong, X.L., Li, G., Song, H.Q., Feng, X.S., Guo, F.: 2013, *Astrophys. J.* **767**, 29. DOI: 10.1088/0004-637X/767/1/29

Gallagher, P.T., Lawrence, G.R., Dennis, B.R.: 2003, *Astrophys. J. Lett.* **588**, L53. DOI: 10.1086/375504

Gary, G.A.: 2001, *Solar Phys.* **203**, 71. DOI: 10.1023/A:1012722021820

Gopalswamy, N., Nitta, N., Akiyama, S., Mäkelä, P., Yashiro, S.: 2012, *Astrophys. J.* **744**, 72. DOI: 10.1088/0004-637X/744/1/72

Grechnev, V.V., Afanasyev, A.N., Uralov, A.M., Chertok, I.M., Eselevich, M.V., Eselevich, V.G., Rudenko, G.V., Kubo, Y.: 2011a, *Solar Phys.* **273**, 461. DOI: 10.1007/s11207-011-9781-y

Grechnev, V.V., Kiselev, V.V., Uralov, A.M., Meshalkina, N.S., Kochanov, A.A.: 2013, *Publ. Astron. Soc. Japan* **65**, SP1, S9. DOI: 10.1093/pasj/65.sp1.S9

Grechnev, V.V., Uralov, A.M., Chertok, I.M., Kuzmenko, I.V., Afanasyev, A.N., Meshalkina, N.S., Kalashnikov, S.S., Kubo, Y.: 2011b, *Solar Phys.* **273**, 433. DOI: 10.1007/s11207-011-9780-z

Grechnev, V.V., Uralov, A.M., Chertok, I.M., Slemzin, V.A., Filippov, B.P., Egorov, Ya.I., Fainshtein, V.G., Afanasyev, A.N., Prestage, N., Temmer, M.: 2014b, *Solar Phys.* **289**, 1279. DOI: 10.1007/s11207-013-0397-2

Grechnev, V.V., Uralov, A.M., Kuzmenko, I.V., Kochanov, A.A., Chertok, I.M., Kalashnikov, S.S.: 2015, *Solar Phys.* **290**, 129. DOI: 10.1007/s11207-014-0621-8

Grechnev, V.V., Uralov, A.M., Slemzin, V.A., Chertok, I.M., Filippov, B.P., Rudenko, G.V., Temmer, M.: 2014a, *Solar Phys.* **289**, 289. DOI: 10.1007/s11207-013-0316-6

Grechnev, V.V., Uralov, A.M., Slemzin, V.A., Chertok, I.M., Kuzmenko, I.V., Shibasaki, K.: 2008b, *Solar Phys.* **253**, 263. DOI: 10.1007/s11207-008-9178-8

Grechnev, V.V., Uralov, A.M., Zandanov, V.G., Baranov, N.Y., Shibasaki, K.: 2006a, *Publ. Astron. Soc. Japan* **58**, 69. DOI: 10.1093/pasj/58.1.69

Grechnev, V.V., Uralov, A.M., Zandanov, V.G., Rudenko, G.V., Borovik, V.N., Grigorieva, I.Y., Slemzin, V.A., Bogachev, S.A., Kuzin, S.V., Zhitnik, I., Pertsov, A.A., Shibasaki, K., Livshits, M.A.: 2006b, *Publ. Astron. Soc. Japan* **58**, 55. DOI: 10.1093/pasj/58.1.55

Hannah, I.G., and Kontar, E.P.: 2012, *Astron. Astrophys.* **539**, A146. DOI: 10.1051/0004-6361/201117576

Hirayama, T.: 1974, *Solar Phys.* **34**, 323. DOI: 10.1007/BF00153671

Howard, R.A., Moses, J.D., Vourlidas, A., Newmark, J.S., Socker, D.G., Plunkett, S.P., Korendyke, C.M., Cook, J.W., Hurley, A., Davila, J.M., *et al.*: 2008, *Space Sci. Rev.* **136**, 67. DOI: 10.1007/s11214-008-9341-4

Hudson, H.S., Webb, D.F.: 1997, in: N. Crooker, J. A. Joselyn, and J. Feynman (eds.), Coronal Mass Ejections. *Washington DC American Geophysical Union Geophysical Monograph Series* **99**, 27. DOI: 10.1029/GM099p0027

Inhester, B., Birn, J., Hesse, M.: 1992, *Solar Phys.* **138**, 257. DOI: 10.1007/BF00151915

Kaiser, M.L., Kucera, T.A., Davila, J.M., St. Cyr, O.C., Guhathakurta, M., Christian, E.: 2008, *Space Sci. Rev.* **136**, 5. DOI: 10.1007/s11214-007-9277-0

Knock, S.A., Cairns, I.H.: 2005, *J. Geophys. Res.* A **110**, A01101. DOI: 10.1029/2004JA010452

Kochanov, A.A., Anfinogentov, S.A., Prosovetsky, D.V., Rudenko, G.V., Grechnev, V.V.: 2013, *Publ. Astron. Soc. Japan* **65**, SP1, S19. DOI: 10.1093/pasj/65.sp1.S19.

Kopp, R.A., Pneuman, G.W.: 1976, *Solar Phys.* **50**, 85. DOI: 10.1007/BF00206193

Kouloumvakos, A., Patsourakos, S., Hillaris, A., Vourlidas, A., Preka-Papadema, P., Moussas, X., Caroubalos, C., Tsitsipis, P., Kontogeorgos, A.: 2014, *Solar Phys.* **289**, 2123. DOI: 10.1007/s11207-013-0460-z

Kozarev, K.A., Korreck, K.E., Lobzin, V.V., Weber, M.A., Schwadron, N.A.: 2011, *Astrophys. J. Lett.* **733**, L25. DOI: 10.1088/2041-8205/733/2/L25

Kundu, M.R., Grechnev, V.V., White, S.M., Schmahl, E.J., Meshalkina, N.S., Kashapova, L.K.: 2009, *Solar Phys.* **260**, 135. DOI: 10.1007/s11207-009-9437-3

Kwon, R.-Y., Ofman, L., Olmedo, O., Kramar, M., Davila, J. M., Thompson, B.J., Cho, K.-S.: 2013, *Astrophys. J.*, **766**, 55. DOI: 10.1088/0004-637X/766/1/55

Kwon, R.-Y., Zhang, J., Olmedo, O.: 2014, *Astrophys. J.* **794**, 148. DOI: 10.1088/0004-637X/794/2/148

Kwon, R.-Y., Zhang, J., Vourlidas, A.: 2015, *Astrophys. J. Lett.* **799**, L29. DOI: 10.1088/2041-8205/799/2/L29

Lemen, J.R., Title, A.M., Akin, D.J., Boerner, P.F., Chou, C., Drake, J.F., Duncan, D.W., Edwards, C.G., Friedlaender, F.M., Heyman, G.F., *et al.*: 2012, *Solar Phys.* **275**, 17. DOI: 10.1007/s11207-011-9776-8

Levenberg, K.: 1944, *Quart. Appl. Math.* **2**, 164.

Livshits, M.A., Badalyan, O.G.: 2004, *Astron. Rep.* **48**, 1037. DOI: 10.1134/1.1836027

Longcope, D.W., Beveridge, C.: 2007, *Astrophys. J.* **669**, 621. DOI: 10.1086/521521

Low, B.C.: 1982, *Astrophys. J.* **254**, 796. DOI: 10.1086/159790

Ma, S., Raymond, J.C., Golub, L., Lin, J., Chen, H., Grigis, P., Testa, P., Long, D.: 2011, *Astrophys. J.* **738**, 160. DOI: 10.1088/0004-637X/738/2/160
Mancuso, S., Raymond, J.C.: 2004, *Astron. Astrophys.* **413**, 363. DOI: 10.1051/0004-6361:20031510
Mandrini, C.H., Pohjolainen, S., Dasso, S., Green, L.M., Démoulin, P., van Driel-Gesztelyi, L., Copperwheat, C., Foley, C.: 2005, *Astron. Astrophys.* **434**, 725. DOI: 10.1051/0004-6361:20041079
Mann, G., Klassen, A., Aurass, H., Classen, H.-T.: 2003, *Astron. Astrophys.* **400**, 329. DOI: 10.1051/0004-6361:20021593
Marquardt, D.W.: 1963, *SIAM J. Appl. Math.* **11**, 431.
Meegan, C., Lichti, G., Bhat, P.N., Bissaldi, E., Briggs, M.S., Connaughton, V., Diehl, R., Fishman, G., Greiner, J., Hoover, A.S., *et al.*: 2009, *Astrophys. J.* **702**, 791. DOI: 10.1088/0004-637X/702/1/791
Meshalkina, N.S., Uralov, A.M., Grechnev, V.V., Altyntsev, A.T., Kashapova, L.K.: 2009, *Publ. Astron. Soc. Japan* **61**, 791. DOI: 10.1093/pasj/61.4.791
Miklenic, C.H., Veronig, A.M., Vršnak, B.: 2009, *Astron. Astrophys.* **499**, 893. DOI: 10.1051/0004-6361/200810947
Neupert, W.M.: 1968, *Astrophys. J. Lett.* **153**, L59. DOI: 10.1086/180220
Patsourakos, S., Vourlidas, A., Stenborg, G.: 2010, *Astrophys. J. Lett.* **724**, L188. DOI: 10.1088/2041-8205/724/2/L188
Plowman, J., Kankelborg, C., Martens, P.: 2013, *Astrophys. J.* **771**, 2. DOI: 10.1088/0004-637X/771/1/2
Qiu, J., Hu, Q., Howard, T.A., Yurchyshyn, V.B.: 2007, *Astrophys. J.* **659**, 758. DOI: 10.1086/512060
Reiner, M.J., Vourlidas, A., St. Cyr, O.C., Burkepile, J.T., Howard, R.A., Kaiser, M.L., Prestage, N.P., Bougeret, J.-L.: 2003, *Astrophys. J.* **590**, 533. DOI: 10.1086/374917
Saito, K.: 1970, *Ann. Tokyo Astr. Obs.* **12**, 53.
Sedov, L.I.: 1981, *Similarity Methods and Dimensional Analysis in Mechanics*, 9th edn., Nauka, Moscow, 448 pp. (in Russian).
Sheeley, N.R., Jr., Warren, H.P., and Wang, Y.-M.: 2007, *Astrophys. J.* **671**, 926. DOI: 10.1086/522940
Smerd, S.F., Sheridan, K.V., Stewart, R.T.: 1974, In: Newkirk, G.A. (ed.) *Coronal Disturbances, IAU Symp.* **57**, Reidel, Dordrecht, 389.
Sterling, A.C., Hudson, H.S.: 1997, *Astrophys. J. Lett.* **491**, L55. DOI: 10.1086/311043
Sturrock, P.A.: 1966, *Nature* **211**, 695. DOI: 10.1038/211695a0
Temmer M., Veronig, A.M., Kontar, E.P., Krucker, S., Vršnak, B.: 2010, *Astrophys. J.* **712**, 1410. DOI: 10.1088/0004-637X/712/2/1410
Temmer, M., Veronig, A.M., Vršnak, Rybák, J., Gömöry, J., Stoiser, S., Maričić, D.: 2008, *Astrophys. J. Lett.* **673**, L95. DOI: 10.1086/527414
Torii, C., Tsukiji, Y., Kobayashi, S., Yoshimi, N., Tanaka, H., Enome, S.: 1979, *Proc. Res. Inst. Atmospherics*, **26**, 129.
Uchida, Y.: 1968, *Solar Phys.* **4**, 30. DOI: 10.1007/BF00146996
Uralov, A.M.: 1990, *Solar Phys.* **127**, 253. DOI: 10.1007/BF00152165
Uralov, A.M., Grechnev, V.V., Hudson, H.S.: 2005, *J. Geophys. Res.* **110**, A05104. DOI: 10.1029/2004JA010951
Uralov, A.M., Grechnev, V.V., Rudenko, G.V., Myshyakov, I.I., Chertok, I.M., Filippov, B.P., Slemzin, V.A.: 2014, *Solar Phys.* **289**, 3747. DOI: 10.1007/s11207-014-0536-4.
Uralov, A.M., Lesovoi, S.V., Zandanov, V.G., Grechnev, V.V.: 2002, *Solar Phys.* **208**, 69. DOI: 10.1023/A:1019610614255
Uralova, S.V., Uralov, A.M.: 1994, *Solar Phys.* **152**, 457. DOI: 10.1007/BF00680450
Vasanth, V., Umapathy, S., Vršnak, B., Žic, T., Prakash, O.: 2014, *Solar Phys.* **289**, 251. DOI: 10.1007/s11207-013-0318-4
Vršnak, B., Maričić, D., Stanger, A.L., Veronig, A.M., Temmer, M., Roša, D.: 2007, *Solar Phys.* **241**, 85. DOI: 10.1007/s11207-006-0290-3
Warmuth, A., Vršnak, B., Aurass, H., Hanslmeier, A.: 2001, *Astrophys. J. Lett.* **560**, L105. DOI: 10.1086/324055
Wang, Y., Zhang, J., Shen, C.: 2009, *J. Geophys. Res.* **114**, 10104. DOI: 10.1029/2009JA014360
Webb, D.F., Lepping, R.P., Burlaga, L.F., DeForest, C.E., Larson, D.E., Martin, S.F., Plunkett, S.P., Rust, D.M.: 2000, *J. Geophys. Res.* **105**, 27251. DOI: 10.1029/2000JA000021
Yashiro, S., Gopalswamy, N., Michalek, G., St. Cyr, O.C., Plunkett, S.P., Rich, N.B., Howard, R.A.: 2004, *J. Geophys. Res.* **109**, A07105. DOI: 10.1029/2003JA010282

Zhang, J., Dere, K.P., Howard, R.A., Kundu, M.R., White, S.M.: 2001, *Astrophys. J.* **559**, 452. DOI: 10.1086/322405